



Measuring Dark Energy Properties with Photometrically Classified Pan-STARRS Supernovae. II. Cosmological Parameters

D. O. Jones¹, D. M. Scolnic^{2,13}, A. G. Riess^{3,4}, A. Rest^{3,4}, R. P. Kirshner^{5,6}, E. Berger⁵, R. Kessler², Y.-C. Pan¹, R. J. Foley¹, R. Chornock⁷, C. A. Ortega³, P. J. Challis⁵, W. S. Burgett⁸, K. C. Chambers⁸, P. W. Draper⁹, H. Flewelling⁸, M. E. Huber⁸, N. Kaiser⁸, R.-P. Kudritzki⁸, N. Metcalfe⁹, J. Tonry⁸, R. J. Wainscoat⁸, C. Waters⁸, E. E. E. Gall^{10,11}, R. Kotak^{10,12}, M. McCrum¹⁰, S. J. Smart¹⁰, and K. W. Smith¹⁰

¹ Department of Astronomy and Astrophysics, University of California, Santa Cruz, CA 92064, USA; david.jones@ucsc.edu

² University of Chicago, Kavli Institute for Cosmological Physics, Chicago, IL, USA

³ Department of Physics and Astronomy, The Johns Hopkins University, Baltimore, MD 21218, USA

⁴ Space Telescope Science Institute, Baltimore, MD 21218, USA

⁵ Harvard-Smithsonian Center for Astrophysics, 60 Garden Street, Cambridge, MA 02138, USA

⁶ Department of Physics, Harvard University, Cambridge, MA 02138, USA

⁷ Astrophysical Institute, Department of Physics and Astronomy, 251B Clipping Lab, Ohio University, Athens, OH 45701, USA

⁸ Institute for Astronomy, University of Hawaii at Manoa, Honolulu, HI 96822, USA

⁹ Department of Physics, Durham University, South Road, Durham DH1 3LE, UK

¹⁰ Astrophysics Research Centre, School of Mathematics and Physics, Queen's University Belfast, Belfast BT7 1NN, UK

¹¹ Max-Planck-Institut für Astrophysik, Karl-Schwarzschild-Str. 1, D-85748 Garching-bei-München, Germany

¹² Tuorlan Observatorio, Väisälantie 20, FI-21500 Piikkiö, Finland

Received 2017 October 2; revised 2018 March 9; accepted 2018 March 12; published 2018 April 12

Abstract

We use 1169 Pan-STARRS supernovae (SNe) and 195 low- z ($z < 0.1$) SNe Ia to measure cosmological parameters. Though most Pan-STARRS SNe lack spectroscopic classifications, in a previous paper we demonstrated that photometrically classified SNe can be used to infer unbiased cosmological parameters by using a Bayesian methodology that marginalizes over core-collapse (CC) SN contamination. Our sample contains nearly twice as many SNe as the largest previous SN Ia compilation. Combining SNe with cosmic microwave background (CMB) constraints from Planck, we measure the dark energy equation-of-state parameter w to be -0.989 ± 0.057 (stat + sys). If w evolves with redshift as $w(a) = w_0 + w_a(1 - a)$, we find $w_0 = -0.912 \pm 0.149$ and $w_a = -0.513 \pm 0.826$. These results are consistent with cosmological parameters from the Joint Light-curve Analysis and the Pantheon sample. We try four different photometric classification priors for Pan-STARRS SNe and two alternate ways of modeling CC SN contamination, finding that no variant gives a w differing by more than 2% from the baseline measurement. The systematic uncertainty on w due to marginalizing over CC SN contamination, $\sigma_w^{\text{CC}} = 0.012$, is the third-smallest source of systematic uncertainty in this work. We find limited (1.6σ) evidence for evolution of the SN color-luminosity relation with redshift, a possible systematic that could constitute a significant uncertainty in future high- z analyses. Our data provide one of the best current constraints on w , demonstrating that samples with $\sim 5\%$ CC SN contamination can give competitive cosmological constraints when the contaminating distribution is marginalized over in a Bayesian framework.

Key words: cosmology: observations – dark energy – supernovae: general

Supporting material: machine-readable tables

1. Introduction

The cause of the universe's accelerating expansion at late times is one of the fundamental questions in astrophysics today. Twenty years ago, distances from Type Ia supernovae (SNe Ia) revealed that the universe was accelerating (Riess et al. 1998; Perlmutter et al. 1999), and the most common interpretation of this cosmic acceleration was that $\sim 70\%$ of the energy in the present-day universe must consist of a repulsive “dark energy.” In the time since this discovery, large SN data sets have compiled up to ~ 750 spectroscopically confirmed SNe Ia and measured the expansion history of the universe at $z \lesssim 1$ with increasing precision (Riess et al. 2004; Hicken et al. 2009b; Kessler et al. 2009; Conley et al. 2011; Sullivan et al. 2011; Suzuki et al. 2012; Betoule et al. 2014; Rest et al. 2014). Because SNe Ia are observed in the recent cosmic epochs when dark energy is most dominant, they have more leverage to

measure dark energy than most other cosmological probes (Weinberg et al. 2013). In conjunction with baryon acoustic oscillation (BAO) and cosmic microwave background (CMB) constraints (e.g., Bennett et al. 2003; Eisenstein et al. 2005; Anderson et al. 2014; Planck Collaboration et al. 2016a), SNe Ia can be used to infer the dark energy equation-of-state parameter w (equal to $P/\rho c^2$, the ratio of pressure to density).

The simplest model of dark energy is a cosmological constant, a vacuum energy that exerts a spatially and temporally constant negative pressure ($w = -1$). However, if w is measured to be greater than -1 , it would be an indication of “quintessence” dark energy, a dynamic scalar field. A w value of less than -1 would imply so-called “phantom” dark energy, which requires extremely exotic physics (Amendola et al. 2013).

Nearly all SNIa analyses have measured a dark energy equation of state consistent with $w = -1$. The most precise measurement to date is that of Betoule et al. (2014, hereafter B14), who combined 740 spectroscopically confirmed SNe Ia from the Sloan Digital Sky Survey (SDSS; Alam et al. 2015), the

¹³ Hubble, KICP Fellow.

SuperNova Legacy Survey (SNLS; Astier et al. 2006), high- z SNe from *HST* (Riess et al. 2007), and low- z SNe (Hamuy et al. 1996; Riess et al. 1999; Jha et al. 2006; Hicken et al. 2009a, 2009b; Contreras et al. 2010; Folatelli et al. 2010) to form the Joint Light-curve Analysis (JLA). JLA SNe Ia, when combined with CMB data from the Planck satellite and BAO constraints from Anderson et al. (2014) and Ross et al. (2015), yield $w = -1.006 \pm 0.045$ (Planck Collaboration et al. 2016a).

Statistical and systematic uncertainties on the JLA measurement of w are approximately equal. Though a great deal of recent progress has been made to lower systematic uncertainties, including the leading systematic of photometric calibration error (Scolnic et al. 2015), lower uncertainties are also possible just by adding more SNe Ia. Although a significant reduction of the statistical uncertainty now requires hundreds of additional SNe Ia, thousands of SNe Ia have already been discovered by Pan-STARRS (PS1; Kaiser et al. 2010). Thousands more are currently being discovered by the Dark Energy Survey (DES; Flaugher 2005), and tens or hundreds of thousands will be discovered by the Large Synoptic Survey Telescope (LSST) in the coming decade.

Obtaining spectroscopic classifications for thousands of SNe is prohibitively expensive. Spectra of SNe Ia cannot be efficiently obtained with multiobject spectroscopy, as they have a sparse density on the sky: their rate is $\sim 10 \text{ yr}^{-1} \text{ deg}^{-2}$ for those with $R \lesssim 22$, and spectral classifications must be obtained within ~ 2 weeks of maximum light. At the median PS1 redshift of $z \sim 0.3$, spectroscopic classifications also necessitate ~ 1 hr or more of 4 m class telescope time per SN. In addition, $\sim 30\%$ of these SNe Ia will fail sample-selection requirements after their spectra have been observed and thus cannot be placed on the Hubble diagram (Section 2.1). Assuming poor weather on $\sim 30\%$ – 50% of nights, 100 nights of 4 m class telescope time will result in a cosmologically useful sample of just ~ 400 SNe Ia. In future surveys, such as LSST, the cost of obtaining spectroscopy for tens of thousands of SNe Ia will far exceed the available resources.

The alternative to spectroscopic classifications is using classifications based only on photometric SN light curves, but this method subjects the sample to contamination by core-collapse (CC) SNe and peculiar SNe Ia. However, if cosmological distances can be measured without bias in a sample with CC SN contamination, photometrically classified SNe Ia could be used to measure w without penalty. To this end, SN light-curve classification algorithms have improved greatly in the last few years. The advent of LSST has provided additional motivation to develop quick, robust classification methods that rely only on limited photometric data (e.g., Saha et al. 2016). Machine-learning algorithms in particular have been found to yield both efficiencies (few bona fide SNe Ia are misclassified) and sample purities $\gtrsim 96\%$ in cases where the classifier can be trained on a representative SN sample (Sako et al. 2014; Lochner et al. 2016).

The first measurement of w with photometrically classified SNe, Campbell et al. (2013), used 752 SDSS SNe, most lacking spectroscopic classifications, to measure cosmological parameters. They reduced CC SN contamination using the PSNID Bayesian light-curve classifier (Sako et al. 2011), among other sample cuts, and estimated that their final sample had 3.9% CC SN contamination. However, Campbell et al. (2013) did not include a systematic uncertainty budget in their measurements. Because CC SNe are 1–2 mag fainter than

SNe Ia, a contamination fraction of just 2% could shift the mean distance by 0.02–0.04 mag, equivalent to a 5%–10% difference in w over the redshift range $0 < z < 0.5$.

For this reason, Kunz et al. (2007) proposed the Bayesian Estimation Applied to Multiple Species (BEAMS) method to simultaneously determine the SN Ia and CC SN distributions. BEAMS models photometrically selected SN samples as a combination of SNe Ia and CC SNe, simultaneously fits for the contributions of each, and marginalizes over nuisance parameters to give cosmological parameter measurements. BEAMS is able to yield cosmological parameter measurements with less bias and nearly optimal uncertainties (Kunz et al. 2007). Hlozek et al. (2012), the first measurement of cosmological parameters from photometrically classified SNe, used the BEAMS method to measure the cosmic matter density Ω_M from SDSS SNe lacking spectroscopic classifications, but again did not include a systematic uncertainty budget in their measurements. However, the case of systematic uncertainties in BEAMS was explored theoretically by Knights et al. (2013), who developed a BEAMS formalism for correlated SN data that gives a reliable cosmological parameter estimation (see also Rubin et al. 2015 for a treatment of systematic uncertainties that includes CC SN contamination).

We expanded on this work in Jones et al. (2017, hereafter J17). J17 undertook a series of Monte Carlo (MC) simulations to test the application of a BEAMS-like algorithm to a PS1 photometrically classified SN sample and made a first estimate of the systematic uncertainty on w due to CC SN contamination. We found a statistically insignificant bias of $\Delta_w^{\text{CC}} = -0.001 \pm 0.004$ and a modest systematic uncertainty of 0.014, which we estimated using four different SN classification methods and three different contamination models. J17 also included SN selection effects (i.e., Malmquist bias), which were not included in the original BEAMS analyses.

In the current work, we apply the J17 methodology to PS1 SNe to measure cosmological parameters with robust systematic uncertainties. Previously, only 10% of PS1 SNe Ia—half of the spectroscopically classified SN Ia sample—had been used to measure cosmological parameters (Rest et al. 2014; Scolnic et al. 2014). The present sample is drawn from 350 spectroscopically classified SNe Ia and 3261 PS1 SNe with spectroscopic host galaxy redshifts. We anchor our Hubble diagram with a compilation of spectroscopically confirmed low- z SNe Ia from the CfA1-4 and Carnegie Supernova Project (CSP) samples (Riess et al. 1999; Jha et al. 2006; Hicken et al. 2009a, 2009b; Contreras et al. 2010; Folatelli et al. 2010; Stritzinger et al. 2011). We exclude SDSS and SNLS SNe from this sample in order to give cosmological constraints that are independent of previous high- z data. After applying conventional light-curve cuts (e.g., B14), we will show that 1364 PS1+low- z SNe remain. Statistically, we expect $\sim 5\%$ of these SNe to be CC SN contaminants (J17).

A companion paper, Scolnic et al. (2017, hereafter S17), compiles 1049 spectroscopically classified SNe Ia from PS1 and other surveys to give cosmological constraints. S17 presents the PS1 spectroscopic sample, including improvements to the PS1 photometric pipeline that are used in this work. This work also relies heavily on the detailed analysis and simulations of the low- z sample in S17 and their improvements to the relative and absolute photometric calibration of all surveys.

The sample of PS1 SNe with host galaxy redshifts was presented in J17, including a description of our campaign to

measure host galaxy redshifts for $\sim 60\%$ of all SN candidates. In Section 2.1, we briefly discuss this sample and present the low- z and PS1 spectroscopically classified SNe that are included in this analysis. We also derive bias-corrected distance measurements and estimate the probability that each SN is Type Ia. In Section 3, we summarize our cosmological parameter estimation methodology, and in Section 4, we discuss contributions to the systematic uncertainty budget. In Section 5, we perform consistency checks on the methodology. In Section 6, we give measurements of Ω_M and w from SN Ia+CMB constraints. In Section 7, we present combined cosmological constraints after combining SNe with CMB, BAO, and local H_0 measurements and compare our constraints to those of B14 and S17. In Section 8, we examine the test case of measuring w from a SN sample without any $z > 0.1$ spectroscopic classifications. Our conclusions are in Section 9.

2. Distances and Photometric Classifications from the SN Data

2.1. Data

The PS1 Medium Deep Survey covers 10.7 deg^2 fields in five filters, with typical observing cadences in a given field of six observations per 10 days. The PS1 SN discovery pipeline is described in detail in Rest et al. (2014). Likely SNe were flagged based on three signal-to-noise ratio (S/N) ≥ 4 observations in the $griz_{PS1}$ filters and no previous detection of a SN at that position. The PS1 survey overview is given in Chambers et al. (2016).

Over its 4 yr of operation, PS1 flagged $\sim 5,200$ likely SNe. Spectroscopic follow-up was triggered for $\sim 10\%$ of SNe, typically those with $r \lesssim 22$ mag, on a wide variety of spectroscopic instruments (see Rest et al. 2014 and S17). For 520 of these candidates, spectroscopic observations of the SN near maximum light allowed their type to be determined, and approximately 350 of these 520 were spectroscopically classified as Type Ia (S17).

During the last year of PS1, we began a survey to obtain spectroscopic host galaxy redshifts for the majority of the sample, both those with SN spectra and those without. This survey primarily used the Hectospec multifiber instrument on the MMT (Fabricant et al. 2005; Mink et al. 2007). We also measured redshifts with the Apache Point Observatory (APO) 3.5 m telescope,¹⁴ the WIYN telescope,¹⁵ and, for two of the most southern medium-deep fields, the Anglo-Australian Telescope (AAT). An additional ~ 600 of our redshifts came from SDSS (Smee et al. 2013) or other public redshift surveys.¹⁶ We chose targets independent of SN type in order to build a sample without any color or shape selection bias. Of 3930 targets, the host galaxies of 3261 SN candidates had strong enough spectral features and high enough S/N to yield reliable spectroscopic redshifts. These data are discussed in detail in J17. We estimate that 1.4% of these redshifts are incorrect, and, as SNe with incorrect redshifts are indistinguishable from CC SNe when placed on the Hubble diagram, the incorrect-redshift fraction will

¹⁴ <http://www.apo.nmsu.edu/arc35m/>

¹⁵ The WIYN Observatory is a joint facility of the University of Wisconsin-Madison, Indiana University, the National Optical Astronomy Observatory, and the University of Missouri.

¹⁶ Public redshifts are from 2dFGRS (Colless et al. 2003), 6dFGS (Jones et al. 2009), DEEP2 (Newman et al. 2013), VIPERS (Scodreggio et al. 2018), VVDS (Le Fèvre et al. 2005), WiggleZ (Blake et al. 2008), and zCOSMOS (Lilly et al. 2007).

contribute to the ‘‘contamination’’ systematic uncertainty for this sample (also discussed in J17).

Though our sample contains a mix of galaxy types (and $\sim 25\%$ of hosts are absorption-line galaxies), we are unable to obtain redshifts for SNe in low surface brightness hosts. Previous high- z SN searches favored SNe in low surface brightness hosts, which allow SN spectra with less host galaxy contamination to be obtained. In the photometrically classified sample, however, including hostless SNe is impossible, and the hosts with spectroscopic redshifts have a median r magnitude of 20.3. Therefore, the preponderance of bright, massive host galaxies gives our sample significantly different SN and host demographics compared to previous high- z data but makes it more similar to the nature of the current low- z sample, which primarily consists of SNe Ia found by targeting bright galaxies.

After SN discovery and redshift follow-up, the PS1 light curves were reprocessed with an enhanced version of the discovery pipeline that included a more realistic (non-Gaussian) point spread function (PSF) model. The PS1 photometric pipeline has been improved further for this analysis and the complementary analysis of S17. The improvements include deeper templates, more accurate astrometric alignment, and better PSF modeling. The zero-point calibration has also been improved by using the Ubcgal process (Padmanabhan et al. 2008; Schlafly et al. 2012). Ubcgal uses repeat observations of stars in PS1 to solve for the system throughput, atmospheric transparency, and detector flat field in the $griz_{PS1}$ filters. It has a photometric accuracy of better than 1% over the entire PS1 3π survey area. Pipeline improvements are discussed in detail in S17.

We use a compilation of low- z SNe observed over the last ~ 20 yr to anchor the Hubble diagram. Nearly all of these SNe are all included in the JLA analysis, including the CfA1-3 SN samples (Riess et al. 1999; Jha et al. 2006; Hicken et al. 2009a, 2009b) and CSP SNe from the first data release (Contreras et al. 2010; Folatelli et al. 2010).¹⁷ We exclude Calan/Tololo SNe (Hamuy et al. 1996), as most lie below the PS1 3π survey area and therefore cannot take advantage of the PS1-based photometric calibration system we use in this paper (Supercal; Scolnic et al. 2015). We also include the most recent CfA SN compilation (CfA4; Hicken et al. 2012) and the second CSP data release (Stritzinger et al. 2011), which were not included in the JLA analysis but are used in the Rest et al. (2014) and S17 PS1 cosmological analyses.

2.2. SALT2 Model

To derive distances from PS1 and low- z SNe, we use the SALT2 light-curve model (Guy et al. 2010, hereafter G10) to measure the light-curve parameters of SNe Ia. We apply the most recent version of SALT2 (SALT2.4), which was retrained by B14 to include additional high- z SNe and improve the photometric calibration.

We then use the measured SALT2 light-curve parameters to restrict our sample to SNe with shapes and colors consistent with normal SNe Ia ($-0.3 < c < 0.3$, $-3 < x_1 < 3$) and well-measured shapes ($\sigma_{x_1} < 1$) and times of maximum light. Although the SALT2 shape and color cuts are slightly asymmetric with respect to the mean of the SNIa populations (Scolnic & Kessler 2016), they are chosen primarily because they are the range within which the SALT2 model is valid. As measuring

¹⁷ See B14 for a detailed description of these data and their respective photometric systems.

Table 1
SALT2-based Data Cuts

	Number of SNe			Comments
	PS1 Host- z	PS1 SN- z	Low- z	
Total candidates	5235
Host Sep $R < 5$	4461	Likely host galaxy can be identified
Good host redshifts	3147
Fit by SALT2	2534	SALT2 parameter fitting succeeds
Not an AGN	2448	174	315	Separated from center or no long-term variability
$-3.0 < x_1 < 3.0$	1938	168	296	SALT2 light-curve shape
$-0.3 < c < 0.3$	1523	160	258	SALT2 light-curve color
$\sigma_{\text{peakMJD}} < 2 \times (1 + z)$	1490	159	254	Uncertainty in time of max. light (rest-frame days)
$\sigma_{x_1} < 1$	1111	147	253	x_1 uncertainty
Fit prob. ≥ 0.001	1053	142	195	χ^2 and N_{dof} -based prob. from SALT2 fitter
Obs. at $t - t_{\text{pk}} > 5$ days	1031	137	195	Observed after maximum at 5 days $< t - t_{\text{pk}} < 45$ days
$E(B-V)_{\text{MW}} < 0.15$	1031	137	195	Milky Way reddening

Note. The host- z column includes all PS1 SNe with the spectroscopic redshift of their host galaxy. The SN- z column includes only spectroscopically classified PS1 SNe without spectroscopic host galaxy redshifts. The reasons for this distinction are due to selection biases and are discussed in Section 2.3.1.

cosmological parameters from SNe without spectroscopic classifications adds the potential for new biases to this work, we also strive for consistency with previous cosmological analyses whenever possible. For this reason, our cuts are nearly identical to those of B14, with two exceptions. The first is that we add a cut on the χ^2 and degrees of freedom of the SALT2 light-curve fit (SALT2 fit probability > 0.001) that was applied by Rest et al. (2014). This cut serves to remove CC SNe, as well as SNe Ia with poor light-curve fits. The second is that we require light curves to have at least one observation > 5 days and < 45 days after maximum, a cut that removes a total of 22 SNe. Without this cut, it is possible that some light-curve fits would have a multi-peaked probability distribution function for several SALT2 light-curve parameters (an issue raised by Dai & Wang 2016). The cuts on x_1 uncertainty and time of maximum light uncertainty also serve to remove the biases that could arise from multi-peaked probability density functions (PDFs). We have not made a similar cut on the color uncertainty; although this uncertainty is often high, it should not bias the SN distances (and any bias would be removed by our bias-correction procedure; Section 2.3.2).

After fitting, we also remove a maximum of two light-curve epochs that lie $> 3\sigma$ from the best-fit SALT2 model. Of the light-curve epochs between -15 days $< t_{\text{max}} < 45$ days, 1.3% are 3 σ outliers. We then rerun SALT2 with these data removed. The purpose of this procedure is to remove photometric data affected by unflagged image or subtraction defects without removing so many data points that CC SN light curves begin to resemble those of SNe Ia. Light-curve outlier removal increases the number of SNe passing the SALT2 fit probability cut by $\sim 10\%$ (giving a slightly larger sample size than the one presented in J17) but does not noticeably increase the CC SN contamination.

The SALT2 cuts (Table 1) reduce the PS1 spectroscopically confirmed SN Ia sample by $\sim 30\%$. They reduce the number of PS1 SNe Ia without spectroscopic classifications by 60%, as these SNe have lower average S/N¹⁸ and a lower fraction with SN Ia-like shapes and colors. Once shape, color, and σ_{x_1} cuts have been applied, the time of maximum uncertainty cut and the fit probability cut remove similar fractions of SNe for both

photometric and spectroscopic samples. The Milky Way extinction cut removes no PS1 SNe, as the medium-deep fields were chosen to be in regions of the sky with low Milky Way $E(B-V)$. The number of SNe remaining after each sample cut is shown in Table 1.

Table 1 also includes selection criteria that apply only to photometrically classified SNe. These include a requirement that the host galaxy can be identified reliably (using the normalized separation between the SN and a galaxy center, R ; Sullivan et al. 2006). We also remove potential active galactic nuclei (AGNs) by discarding SN candidates with both evidence for long-term variability and positions within $0''.5$ of their host centers.

Once the light-curve parameters have been measured by using the SNANA fitting program to implement the SALT2 model, we use the Tripp estimator (Tripp 1998) to infer the SN distance modulus from these light-curve parameters:

$$\mu = m_B - \mathcal{M} + \alpha \times x_1 - \beta \times c + \Delta_M + \Delta_B. \quad (1)$$

Here x_1 is the light-curve stretch parameter, c is the light-curve color parameter, and m_B is the log of the light-curve amplitude (approximately the peak SN magnitude in B). The distance to a given SN also depends on the global nuisance parameters α , β , and \mathcal{M} . \mathcal{M} —a combination of the absolute SN magnitude and the Hubble constant $-\alpha$, and β is typically marginalized over when fitting to the cosmological parameters (e.g., B14; Conley et al. 2011). The parameter Δ_M is a correction based on the mass of the SN host galaxy, discussed in Section 2.2.1, and Δ_B is the distance bias correction, caused by SN selection effects. We use simulations to determine an initial Δ_B and apply it to the data (Section 2.3.2) before measuring α , β , and Δ_M . After α and β have been measured, we redetermine Δ_B using the measured α and β as input in the simulations. The simulated/measured α and β are given in Section 6.

After light-curve fitting with the SALT2 model, even SNe Ia with low photometric uncertainties have a $\gtrsim 10\%$ scatter in shape- and color-corrected magnitude. This is traditionally referred to as the intrinsic dispersion, σ_{int} (Guy et al. 2007), which is defined as the global uncertainty that must be added in quadrature to the distance errors σ_μ of each SN such that the reduced χ^2 of the Hubble residuals equals 1. This is not added to the uncertainty but kept as a free parameter in the

¹⁸ These SNe more frequently fail the shape uncertainty cut. In PS1, SNe with x_1 uncertainty < 1 have a mean S/N at maximum light of 15.6. SNe with x_1 uncertainty > 1 have a mean S/N at maximum light of 8.3.

cosmological parameter estimation. The SN Ia uncertainties also include redshift uncertainty and lensing uncertainty ($\sigma_{\text{lens}} = 0.055z$; Jönsson et al. 2010).

2.2.1. Host Galaxy Masses

It has been shown that after shape and color correction, SNe Ia are ~ 0.05 – 0.1 mag brighter in high-mass host galaxies ($\log(M_*/M_\odot) > 10$) than in lower-mass host galaxies at the same redshifts (Δ_M ; Kelly et al. 2010; Lampeitl et al. 2010; Sullivan et al. 2010). The Δ_M parameter has recently been measured at $>3\sigma$ significance in photometrically classified SN samples, even though such samples (including PS1) have strong selection biases toward high-mass host galaxies (Campbell et al. 2016; Wolf et al. 2016; Uddin et al. 2017). Although the underlying physics behind the mass step are unclear, a simple step function appears to fit the SN data well (B14).

Computing Δ_M robustly requires measuring the host galaxy masses of every SN in a self-consistent way. We therefore measured host masses using the spectral energy distribution- (SED-) fitting method of Pan et al. (2014) with PS1 and low- z host galaxy photometry. For the low- z sample, we use *ugriz BVRJHK* photometry from 2MASS (Skrutskie et al. 2006) and SDSS. For PS1, we use SExtractor (Bertin & Arnouts 1996) to measure the photometry from PS1 templates. The PS1 templates are comprised of ~ 3 yr of co-added PS1 data, omitting only the year in which the SN Ia occurred.

The likely host of each SN is assumed to be the galaxy with the lowest R parameter relative to the SN position, as discussed in J17. The R parameter defines a separation between the SN and a galaxy center and is normalized by the size of the galaxy in the direction of the SN.¹⁹ If the nearest host has $R > 5$ (i.e., the SN spectrum gives the only redshift), we assume the true host was undetected following Sullivan et al. (2006).

We use the low- z and PS1 host galaxy photometry to estimate M_* with the Z-PEG SED-fitting code (Le Borgne & Rocca-Volmerange 2002), which in turn is based on spectral synthesis models from PEGASE.2 (Fioc & Rocca-Volmerange 1997). Galaxy SED templates correspond to spectral types SB, Im, Sd, Sc, Sbc, Sa, S0, and E. We simultaneously marginalize over $E(B-V)$, which is allowed to vary from 0 to 0.2 mag. Uncertainties are determined from the range of model parameters that are able to fit the data with similar χ^2 and are typically ~ 0.1 – 0.3 dex.

Undetected galaxies of spectroscopically classified SNe Ia are placed in the $\log(M_*/M_\odot) < 10$ bin. At $z \gtrsim 0.5$, we cannot be sure that SN hosts have $\log(M_*/M_\odot) < 10$, and we therefore add a systematic uncertainty of 0.07 mag in quadrature to those distance uncertainties (similar to B14).

2.3. SN Selection Bias

2.3.1. Simulating PS1 and Low- z SNe

A magnitude-limited sample of SNe will have a distance bias, caused by SN selection effects, that can be determined from rigorous simulations of the survey (see, e.g., B14; Conley et al. 2011; Scolnic et al. 2014). We use the SNANA software (Kessler et al. 2010) to simulate SNe Ia based on the SALT2 model, with detection efficiencies, zero points, PSF sizes, sky

noise, and other observables from the real PS1 and low- z surveys. We generate the simulations using the values of α and β measured from our data as input ($\alpha = 0.161$ and $\beta = 3.060$; Section 5).

We use three survey simulations in this analysis: simulations of the set of PS1 SNe with redshifts from their host galaxies (the host- z sample), the set of PS1 SNe Ia without host redshifts and with only redshifts from SN spectroscopy (the SN- z sample; these SNe have also been spectroscopically classified), and the compilation of low- z SNe Ia. It is important that we use distinct simulations for SNe with and without host redshifts; because SN spectroscopy is only attempted for bright SNe ($r_{\text{pk}} \lesssim 22$), a lower magnitude limit than the PS1 survey detection limit comes into play for the SN- z sample. The SN- z sample includes only the portion of our data without host galaxy redshifts and thus is comprised almost entirely of $r_{\text{pk}} < 22$, spectroscopically classified SNe in faint hosts ($r_{\text{host}} \gtrsim 22$). On the other hand, the host- z sample is nearly an ideal, magnitude-limited SN sample, but it consists only of SNe in brighter ($r \lesssim 22$ – 23) hosts. Even after shape and color correction, SN Ia luminosity is a function of the biased host galaxy properties in these samples, and we must correct for these biases using the Δ_M parameter (variants given in the systematic error analysis; Section 4). All PS1 simulations include photometric noise from the host galaxy, as discussed in J17. Simulations of the PS1 host- z sample are presented in J17 (including CC SN contamination, which we discuss in detail in J17), while the SN- z and low- z samples are presented in S17. The sizes of each of the three SN subsamples are given in Table 1.

The host- z sample is also host galaxy magnitude-limited. Because SN shape and color correlate with host galaxy brightness (e.g., Childress et al. 2013), the SN shape and color distribution in the host- z sample have a z dependence that is difficult to model. Similarly, the SN- z sample consists of spectroscopically classified SNe for which host galaxy redshifts could not be measured, and therefore it will also have a biased, z -dependent host galaxy distribution. Because of this, we add one additional component to the host- z and SN- z simulations: we allow the means of the simulated SALT2 parameters x_1 and c to evolve slightly with redshift to better match the data. We discuss the details and impact of this method in the Appendix and find that it changes the distance bias by up to ~ 20 mmag in the highest redshift bins but by less than 5 mmag on average.

The low- z surveys are exceptionally difficult to model due to their heterogeneous nature, multiple photometric systems and analysis pipelines, semi-arbitrary spectroscopic selection functions, and targeting of NGC galaxies. Furthermore, the cadence and depth of the search are often unknown. Because of this, we simulate both a “magnitude-limited” variant and a “volume-limited” variant of the low- z survey. We treat the magnitude-limited variant as the baseline simulation for bias corrections. The volume-limited variant matches the observed data with a “host galaxy targeting” selection function—the fraction of hosts observed as a function of redshift—instead of a “spectroscopic follow-up” selection function (the fraction of SNe followed as a function of magnitude). Similarly to the PS1 simulations, we use redshift-dependent x_1 and c distributions due to the redshift-dependent host galaxy properties (x_1/c and host properties are correlated; Childress et al. 2013). These simulations are discussed in more detail in S17.

¹⁹ We predict that for $\sim 1\%$ of SNe, this method will incorrectly determine the host galaxy, but in J17, we determined that this fraction of mismatches does not bias the cosmology.

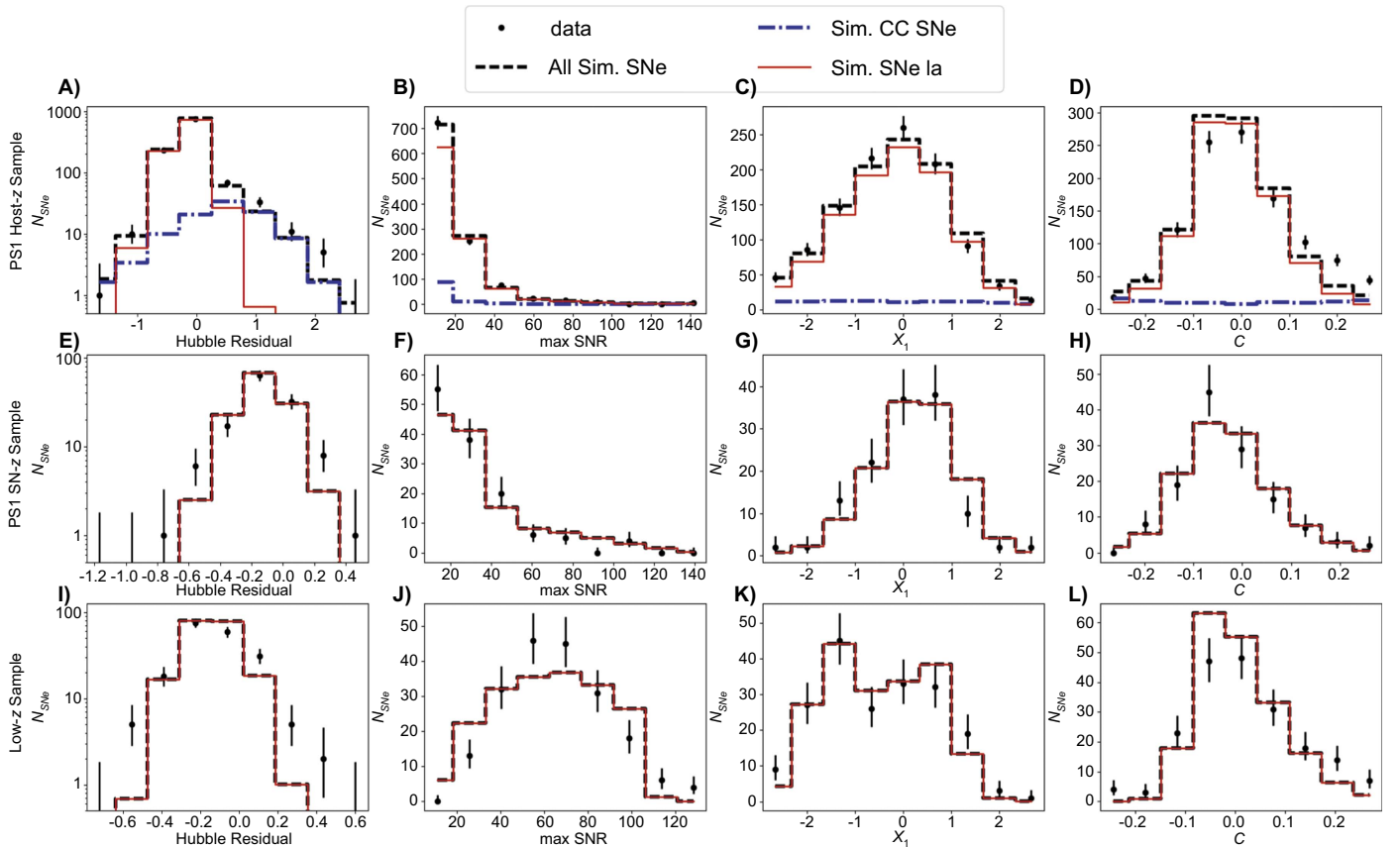


Figure 1. Simulations of the PS1 host galaxy redshift sample (host- z sample), PS1 SN redshift sample (SN- z sample), and low- z SN sample compared to the real SNe used to measure cosmological parameters in this work. The PS1 host- z sample consists of $\sim 9\%$ CC SN contamination, the details of which are discussed in J17 (CC SN contamination is not relevant for distance bias correction).

For each survey, the simulations are compared to the data in Figures 1 and 2. The distributions of x_1 , c , and their redshift dependences are consistent with the data, as is the distribution of SN S/Ns at maximum light. Discrepancies on the red tail of the c distribution could be due to small inaccuracies in the CC SN simulations (J17). The biggest discrepancies between the simulations and data are found in the low- z simulations due to the difficulty of modeling those searches and follow-up programs, as discussed above.

2.3.2. Using Simulations to Correct for Selection Bias

Due to their intrinsic dispersion, SNeIa discovered in magnitude-limited surveys appear increasingly luminous at greater distance—even after shape and color correction. Even the low- z SNeIa surveys used here may be biased toward preferentially selecting brighter SNeIa for spectroscopic follow-up (see B14, their Figure 5). The bias in distance is given by the SNANA simulations discussed above and is defined by (Mosher et al. 2014)

$$\Delta_B(z) = \langle \mu_{\text{fit}} - \mu_{\text{sim}} \rangle_z. \quad (2)$$

For low- z surveys, the bias can be up to ~ 0.035 mag ($z > 0.05$), while PS1 has distance biases of nearly 0.1 mag at $z > 0.5$.

Uncertainty in the intrinsic dispersion model is the dominant uncertainty in the bias corrections. The uncertainty is encapsulated by two primary scatter models that are both consistent with the data. First, the G10 SALT2 model assumes

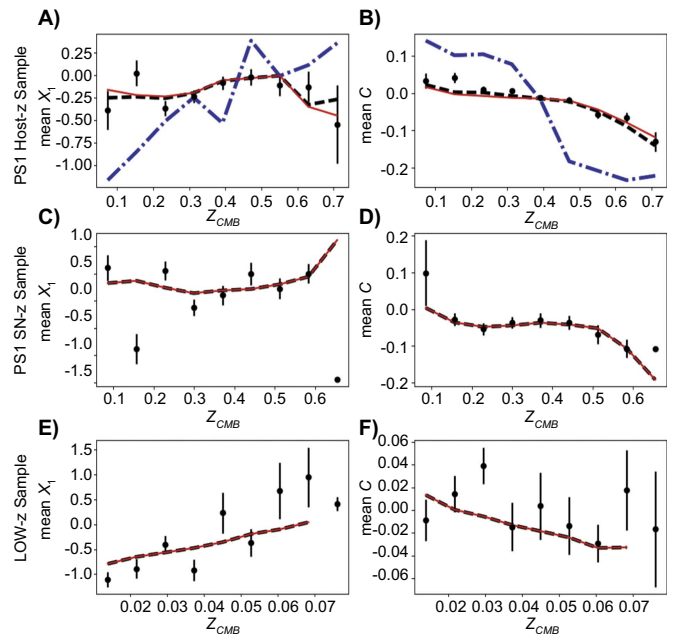


Figure 2. Similar to Figure 1 (see Figure 1 legend) but showing the dependence of x_1 and c on redshift for each survey.

that 70% of the ~ 0.1 mag intrinsic dispersion in derived SNeIa distances is uncorrelated with the shape or color of the SN (achromatic dispersion). An alternative model is that of Chotard et al. (2011, hereafter C11). C11 found an equally

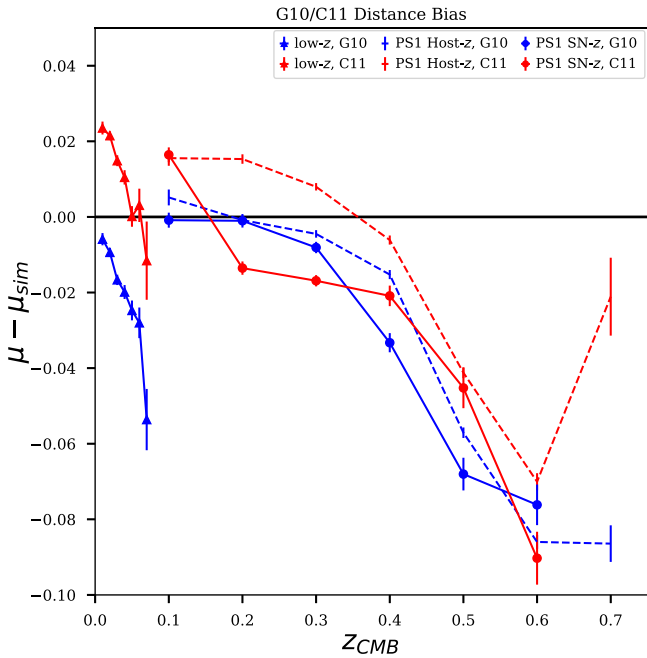


Figure 3. Difference in SN Ia distance bias for the **G10** and **C11** scatter models. Low- z SNe have a bias of up to 0.035 mag, while PS1 SNe have a bias of up to ~ 0.1 mag at the highest survey redshifts. At the highest survey redshifts, where few SNe Ia can be discovered, the **C11** model predicts a drastically different bias from that of the **G10** model due to selection and measurement biases in the SALT2 c parameter.

good fit to SN data by assuming 75% of SN dispersion can be attributed to chromatic variation.

The host- z and SN- z biases are very similar, which is surprising given that SNe in the SN- z sample are much brighter, on average, than those in the host- z sample. The reason is that the lower average S/N of the host- z sample exacerbates a bias caused by the x_1 uncertainty cut. At a given S/N, SNe with narrower (measured) light-curve shapes are given lower x_1 uncertainties by SALT2. This introduces a nonintuitive bias in the case where many x_1 uncertainties are near the cutoff point (for inclusion in our sample) of $\sigma_{x_1} = 1$. As discussed in J17 (Figure 8), a $\sigma_{x_1} < 1$ sample cut biases the recovered values of x_1 by up to $\alpha(x_1 - x_{1,\text{sim}}) = -0.1$ at high- z . The size of this bias is similar to the size of the m_B bias of spectroscopically confirmed SNe Ia (~ 0.05 mag at $z \sim 0.5$).

The SALT2 nuisance parameter β is 25% higher in the **C11** model than in the **G10** model (Scolnic & Kessler 2016), and these two models can give very different predictions for the distance bias as a function of redshift (Figure 3). Due to the chromatic nature of the **C11** dispersion, the **C11** bias is a strong function of the (z -dependent) SN c distribution in a given survey. This is especially apparent when examining the difference between the **G10/C11** biases for the different samples. Low- z and photometrically classified SNe have a median c between -0.01 and 0.01 , giving an average $\beta^{C11}c - \beta^{G10}c = 0.015$ mag for low- z and 0.003 mag for PS1 photometrically classified SNe. In contrast, PS1 spectroscopically confirmed SNe Ia have a median c of -0.04 , giving an average difference of $\beta^{C11}c - \beta^{G10}c = -0.028$ mag in distance. Unfortunately, there are not enough spectroscopically classified SNe Ia to distinguish between the **G10/C11** scatter models in our data, and the differences between these two

model predictions will contribute to our systematic error budget.

2.4. Photometric Classification

In the previous sections, we made SALT2-based cuts and distance bias corrections to our data without requiring any knowledge as to which of the SNe in the photometrically classified sample were SNe Ia. We now use PSNID (Sako et al. 2014) to classify each SN in this sample as Type Ia, Ib/c, or II based on its light curve. PSNID matches observed SN light curves to simulated SN Ia and CC SN light curves. The comparison of data to templates gives a χ^2 and prior-based probability that a given SN is Type Ia. We use the version of PSNID that has been implemented in SNANA.²⁰ For SNe Ia, we use the SALT2 model as the PSNID SN Ia template, and for CC SNe, PSNID marginalizes over 51 CC SN templates when classifying SNe. We include a grid of host galaxy reddening values for each template (because templates have not been corrected for host galaxy reddening, we allow just $0 < A_V < 1$ of additional reddening).

Although PSNID classifications will be used for the baseline version of our cosmological analysis (Section 3), we also use three alternate classification methods. These include two light-curve-based methods, nearest neighbor (NN; Sako et al. 2014; Kessler & Scolnic 2017) and *Fitprob*. The NN classifier uses the proximity of SN light-curve parameters to the SALT2 x_1 , c , and redshift of simulated CC and Ia SNe to determine the likely SN type. *Fitprob* is the fit probability from the SALT2 light-curve fit multiplied by a redshift-dependent SN type prior. This prior is based on simulations, which give the expected fractions of CC SNe and SNe Ia at each redshift (J17, Appendix B). One additional method, GalSNID (Foley & Mandel 2013; J17), takes advantage of the paucity of CC SNe in low star formation environments to estimate the SN type probability from only host galaxy properties. *Fitprob* and GalSNID are less accurate classifiers (J17) but are also less subject to the uncertainties in CC SN simulations. In J17, we suggest that uncertainties in the shape of CC SN luminosity functions and the dearth of CC SN templates for several subtypes necessitate the use of methods that are less reliant on simulations.

Figure 4 shows the classification probabilities for three PS1 SNe with ambiguous types. For SN 570024 (top panel), two of three light-curve-based classification methods agree that this SN is most likely a CC SN due to its poor SALT2 model fit in the z -band. GalSNID, however, finds that this is most likely a bona fide Ia due to the lack of strong star formation indicators in its host galaxy spectrum. For SN 500025 (middle panel), PSNID and *Fitprob* agree that the SN is of Type Ia due to the low χ^2 of its light-curve fit. However, the NN classifier finds it most likely to be a CC SN due to its red SALT2 color. For SN 550152 (bottom panel), the shapes/colors are consistent with a SN Ia, but the light-curve fit χ^2 is too high to definitively prefer a SN Ia. This diversity in classification methodologies and outcomes will help our systematic uncertainty budget to account for the possibility of cosmological bias due to mistyped SNe.

Figure 5 illustrates the classification probabilities. We show the PS1 Hubble residual histograms for likely SNe Ia and CC SNe without spectroscopic classifications as determined by each of the four classification methods considered in this work.

²⁰ Version 10.52g.

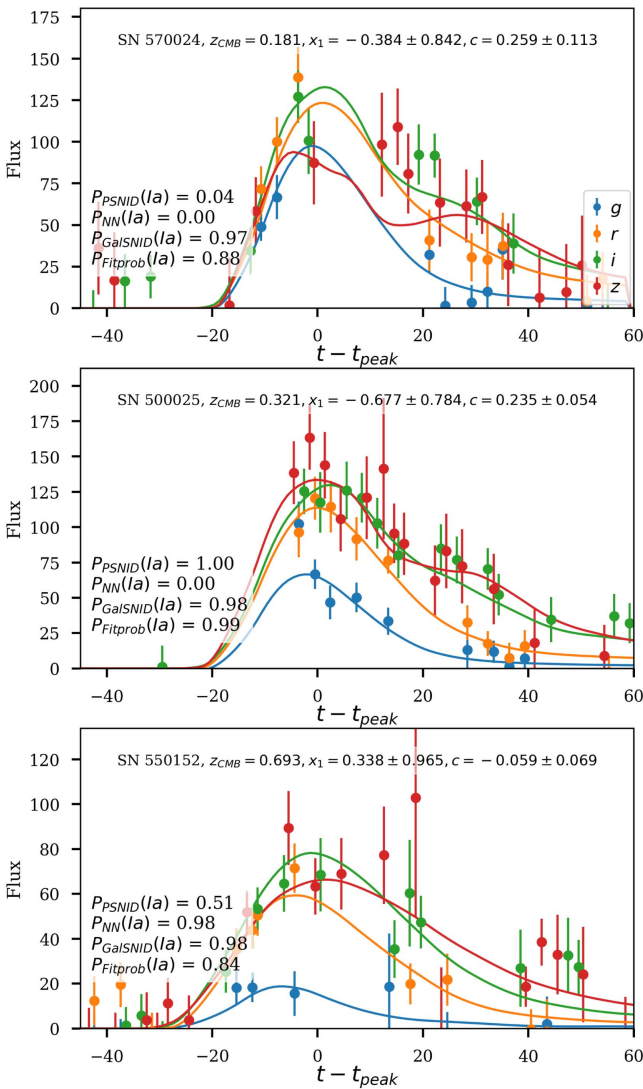


Figure 4. Three PS1 light curves with ambiguous classifications included in our sample. The curves show their best-fit SALT2 light-curve fits.

As a diagnostic, if we assume all SNe with Hubble residual >1 are CC SNe, we find that PSNID classifies 80% of these CC SNe correctly, while NN classifies 60% correctly. *Fitprob* and GalSNID classify 70% and 20% correctly, respectively. We note that PSNID is unable to classify all SNe, rejecting 13 as too noisy or uncertain for classification. We revisit the effect of different classifiers on our results in Section 5.

3. Cosmological Parameter Estimation Methodology

In the previous section, we measured the SALT2 light-curve parameters, host galaxy masses, SN type probabilities, and bias corrections that will be used to generate distances from PS1 and low- z SNe Ia. For each SN in our final sample, these parameters are given in Table 2. Host galaxy coordinates and redshift information are given in Table 3. Light curves and host galaxy spectra are available at <https://doi.org/10.17909/T95Q4X>. From this point forward, we use all PS1 and low- z data combined—data with and without spectroscopic classifications—to obtain the best possible measurements of cosmological parameters. We use the PSNID classifications to generate our baseline, statistics-only cosmological parameter measurements

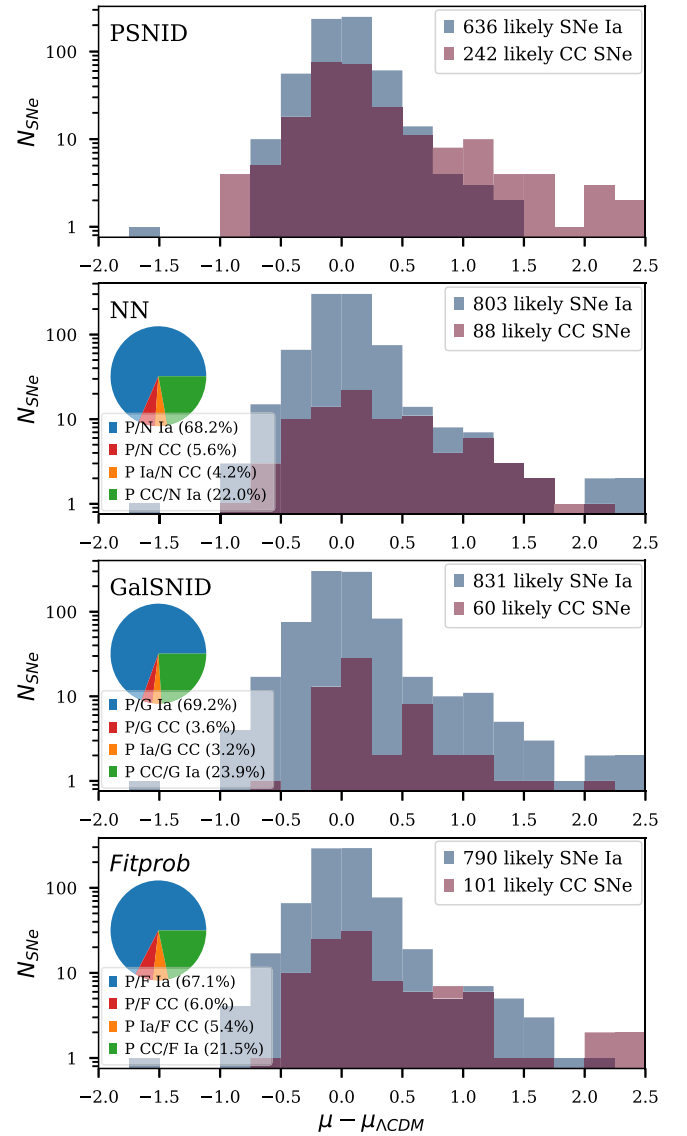


Figure 5. For SNe without spectroscopic classifications, log-scaled histograms of Hubble residuals for likely PS1 SNe Ia ($P(Ia) > 0.5$; blue) and likely PS1 CC SNe ($P(Ia) < 0.5$; red) from each classifier considered in this work. *Fitprob* classifies the most real SNe Ia as CC SNe, while GalSNID likely classifies the most real CC SNe as SNe Ia. In spite of large classification differences, the SN Ia distances given by different classifiers will be shown to be consistent with each other and with the spectroscopically confirmed PS1 sample (Section 5). The pie charts show the level of agreement/disagreement between each classifier and PSNID, where P, N, G, and F indicate PSNID, NN, GalSNID, and *Fitprob* classifications. In these pie charts, we label SNe with $P(Ia) > 0.5$ as Ia and SNe with $P(Ia) < 0.5$ as CC.

and incorporate the other classification methods into our systematic uncertainty budget. To reduce CC SN contamination, we apply one additional cut on a classifier-by-classifier basis before estimating cosmological parameters: we remove SNe with $P(Ia) < 0.5$. Therefore, 1109 likely SNe Ia will be used in our baseline cosmological analysis, and between 1263 and 1304 SNe will be used for the alternate classification methods.

For some readers, the most interesting question might be whether future cosmological analyses, such as those of DES or LSST, can robustly measure w without a spectroscopically classified SN sample as part of the data. We explore this question in Section 8.

Table 2
PS1 Coordinates and Light-curve Parameters

SN	α	δ	$z_{\text{CMB}}^{\text{SN}}$	$z_{\text{CMB}}^{\text{Host}}$	t_{peak}	x_1	c	m_B	$P_{\text{PSNID}}(\text{Ia})^{\text{a}}$	$\log(M_{\text{Host}}/M_{\odot})$
010196	12:16:49.602	46:14:06.33	...	0.369	55246.40(0.20)	-1.457(0.876)	0.228(0.075)	22.970(0.076)	...	11.192(0.155)
010203	08:40:02.784	43:26:32.85	0.088	0.087	55230.60(0.10)	1.234(0.163)	-0.061(0.028)	18.135(0.046)	...	10.384(0.009)
010204	08:41:36.065	43:24:02.18	0.477	0.477	55241.10(0.40)	-1.727(0.839)	-0.032(0.048)	22.841(0.015)	0.9957	10.519(0.315)
010218	09:54:32.47	01:56:37.53	...	0.577	55248.70(0.50)	0.509(0.768)	-0.098(0.056)	23.212(-0.002)	0.8756	9.737(0.151)
010222	12:16:56.796	47:17:21.68	...	0.408	55241.30(0.40)	0.139(0.523)	0.028(0.036)	22.386(0.024)	0.9998	10.164(0.301)
010230	12:21:10.815	47:48:13.43	...	0.303	55246.30(0.40)	-0.659(0.362)	-0.042(0.035)	21.768(0.043)	1.0000	10.395(0.157)
010430	08:45:12.962	43:52:36.68	...	0.327	55258.20(0.50)	-1.447(0.428)	-0.029(0.068)	21.886(0.090)	0.9622	12.070(0.194)
020026	12:15:12.803	46:02:40.40	...	0.321	55276.60(0.40)	0.314(0.325)	-0.127(0.031)	21.485(0.036)	1.0000	10.824(0.041)
020033	12:17:03.99	46:04:22.76	...	0.530	55268.50(1.50)	-0.888(0.962)	-0.065(0.074)	22.858(0.041)	...	11.737(0.013)
020034	12:18:12.126	46:05:10.35	...	0.199	55272.10(0.30)	-1.165(0.431)	0.085(0.034)	20.828(0.042)	...	11.037(0.049)
020047	09:56:56.438	01:36:49.80	...	0.266	55260.20(0.80)	-0.952(0.884)	0.111(0.151)	22.832(0.224)	0.9850	10.528(0.150)
020075	14:18:54.904	53:59:57.08	0.156	0.157	55286.80(0.40)	2.350(0.465)	0.207(0.053)	21.395(0.085)	...	8.795(0.217)
020104	09:58:36.773	02:17:37.70	...	0.306	55277.10(0.60)	0.701(0.533)	-0.080(0.026)	21.507(0.040)	0.9314	10.905(0.257)
020123	12:22:25.600	48:02:28.66	...	0.498	55265.30(1.40)	-0.668(0.967)	-0.018(0.087)	22.856(0.062)	0.9915	10.532(0.382)
020148	10:38:21.978	57:23:24.30	0.102	0.102	55259.70(0.20)	-1.103(0.241)	-0.023(0.036)	18.980(0.059)	...	11.306(0.065)
020194	09:58:34.811	00:49:52.10	...	0.246	55277.90(0.50)	-1.012(0.734)	0.079(0.058)	21.420(0.069)	...	10.965(0.133)
020198	10:46:52.536	57:07:45.51	0.361	0.361	55286.20(0.70)	-0.805(0.891)	-0.083(0.081)	22.284(0.119)	0.5443	10.034(0.033)
020200	14:12:11.636	53:27:47.48	0.116	0.116	55291.10(0.20)	0.005(0.166)	0.110(0.037)	20.513(0.062)	...	10.400(0.186)
030005	12:25:23.414	47:29:11.16	...	0.420	55284.70(0.60)	-1.345(0.617)	-0.002(0.076)	22.315(0.083)	0.9810	11.270(0.018)
030007	14:09:23.651	53:37:06.96	...	0.260	55293.80(0.40)	-0.669(0.337)	0.067(0.050)	21.516(0.076)	1.0000	10.030(0.279)
030068	12:14:39.906	48:05:21.86	...	0.296	55294.70(0.30)	-0.310(0.789)	-0.012(0.076)	22.474(0.096)	0.9989	11.457(0.102)
030216	14:14:56.573	54:12:41.36	...	0.198	55304.10(0.90)	-2.157(0.532)	0.010(0.041)	21.768(0.069)	...	10.799(0.094)
030245	12:26:08.645	46:30:52.82	...	0.581	55290.20(0.80)	-0.633(0.686)	-0.188(0.076)	22.748(0.017)	1.0000	10.450(0.451)
030252	12:17:28.972	48:05:38.05	...	0.326	55319.10(0.60)	0.746(0.552)	0.094(0.055)	22.240(0.091)	1.0000	8.784(0.193)
030263	12:20:47.701	48:10:01.13	...	0.299	55312.00(0.20)	0.717(0.275)	-0.049(0.030)	21.168(0.047)	1.0000	10.116(0.310)
040121	10:39:04.003	58:35:25.74	...	0.322	55309.50(0.40)	0.561(0.368)	-0.030(0.038)	21.527(0.049)	1.0000	9.409(0.281)
040139	14:17:09.899	53:05:11.39	...	0.267	55324.30(0.90)	-0.211(0.306)	0.146(0.036)	21.599(0.057)	1.0000	10.224(0.281)
040147	14:15:40.447	54:13:43.85	...	0.244	55317.40(0.40)	-0.927(0.293)	0.100(0.043)	21.316(0.073)	...	10.459(0.148)
040151	12:21:49.674	46:27:04.69	...	0.256	55326.30(0.20)	-1.576(0.326)	0.014(0.032)	21.473(0.043)	1.0000	11.207(0.015)
040163	12:22:04.649	47:00:36.58	...	0.416	55321.30(0.20)	-0.248(0.470)	-0.070(0.051)	22.302(0.046)	1.0000	9.822(0.632)
040168	12:27:10.791	47:11:23.08	...	0.206	55325.00(0.20)	-0.342(0.541)	0.106(0.047)	20.953(0.053)	...	10.898(0.084)
040169	10:49:29.313	58:45:59.05	...	0.421	55332.60(0.30)	0.208(0.937)	-0.009(0.064)	22.716(0.059)	0.6477	10.609(0.241)
040170	12:14:21.336	47:50:35.25	...	0.190	55330.40(0.30)	-0.935(0.187)	-0.009(0.028)	20.484(0.039)	...	11.449(0.046)
040176	12:20:58.358	45:56:04.95	...	0.348	55327.30(1.70)	1.351(0.778)	0.025(0.042)	21.788(0.047)	1.0000	10.992(0.053)
040313	12:16:25.19	48:21:56.92	...	0.266	55335.80(0.60)	-0.394(0.727)	0.235(0.056)	22.598(0.083)	0.9996	9.791(0.105)
040316	14:11:23.481	52:26:04.60	...	0.443	55324.00(0.20)	0.286(0.782)	0.216(0.075)	22.913(0.054)	0.6527	10.464(0.140)
040318	14:17:19.799	53:06:45.28	...	0.300	55334.40(0.20)	0.109(0.617)	-0.013(0.050)	22.065(0.062)	0.6791	10.588(0.272)
040343	10:39:09.733	58:40:39.35	...	0.343	55334.00(0.70)	-0.019(0.645)	0.107(0.055)	22.250(0.055)	0.9789	10.898(0.022)
040377	10:40:51.886	58:52:53.50	...	0.352	55302.40(1.10)	1.248(0.629)	0.125(0.067)	22.158(0.071)	0.9959	9.750(0.467)
040434	12:21:24.625	45:53:41.62	...	0.654	55315.60(0.90)	-1.624(0.838)	-0.059(0.089)	23.100(0.048)	...	10.861(0.018)
040473	10:58:22.122	58:28:59.27	...	0.161	55302.60(1.40)	0.056(0.571)	-0.007(0.130)	19.982(0.146)	...	10.964(0.029)
040477	16:20:34.012	54:48:24.17	...	0.346	55332.00(0.60)	0.696(0.418)	-0.023(0.032)	21.532(0.031)	1.0000	11.003(0.037)

Note.

^a P(Ia) probabilities used in the likelihood model. These are set to P(Ia) = 1 for spectroscopically classified SNe Ia and the probabilities given by PSNID for photometrically classified SNe. SNe without a P(Ia) were unable to be classified by PSNID.

(This table is available in its entirety in machine-readable form.)

Table 3
PS1 Host Galaxies

SN	Host α	Host δ	$z_{\text{CMB}}^{\text{Host}}$	Normalized Sep. ^a	T&D R^b	z_{source}
010196	12:16:49.577	46:14:06.27	0.369	0.624	7.340	MMT/Hecto
010203	08:40:02.725	43:26:33.14	0.087	1.044	23.880	MMT/Hecto
010204	08:41:36.025	43:24:02.56	0.477	1.741	8.080	MMT/Hecto
010218	09:54:32.455	01:56:38.21	0.577	2.468	4.280	MMT/Hecto
010222	12:16:56.817	47:17:22.39	0.408	1.777	7.280	MMT/Hecto
010230	12:21:10.792	47:48:13.10	0.303	1.413	9.420	MMT/Hecto
010430	08:45:12.976	43:52:38.13	0.327	1.440	...	SDSS
020026	12:15:12.784	46:02:41.30	0.321	1.287	5.040	MMT/Hecto
020033	12:17:04.116	46:04:20.33	0.530	2.815	8.830	MMT/Hecto
020034	12:18:12.000	46:05:10.87	0.199	1.525	7.380	MMT/Hecto
020047	09:56:56.503	01:36:49.99	0.266	1.103	4.200	MMT/Hecto
020075	14:18:54.883	53:59:57.18	0.157	1.780	13.710	MMT/Hecto
020104	09:58:36.813	02:17:37.53	0.306	0.119	14.020	MMT/Hecto
020123	12:22:25.692	48:02:29.95	0.498	2.874	4.190	MMT/Hecto
020148	10:38:21.820	57:23:23.82	0.102	0.683	...	SDSS
020194	09:58:34.812	00:49:51.78	0.246	0.393	8.830	MMT/Hecto
020198	10:46:52.540	57:07:45.40	0.361	0.448	12.460	MMT/Hecto
020200	14:12:11.216	53:27:50.95	0.116	3.171	18.190	MMT/Hecto
030005	12:25:23.424	47:29:10.85	0.420	0.523	7.480	MMT/Hecto
030007	14:09:23.635	53:37:07.06	0.260	1.275	11.920	MMT/Hecto
030068	12:14:39.72	48:05:22.10	0.296	2.365	8.320	MMT/Hecto
030216	14:14:56.627	54:12:43.21	0.198	1.582	8.360	MMT/Hecto
030245	12:26:08.666	46:30:52.84	0.581	0.785	4.610	WIYN/Hydra
030252	12:17:28.923	48:05:38.05	0.326	2.510	6.510	WIYN/Hydra
030263	12:20:47.774	48:10:00.74	0.299	0.370	4.970	MMT/Hecto
040121	10:39:03.921	58:35:27.14	0.322	1.853	4.550	MMT/Hecto
040139	14:17:09.885	53:05:11.20	0.267	0.864	23.550	MMT/Hecto
040147	14:15:40.454	54:13:43.82	0.244	0.194	8.630	MMT/Hecto
040151	12:21:49.768	46:27:06.13	0.256	2.506	16.440	MMT/Hecto
040163	12:22:04.663	47:00:37.89	0.416	2.993	5.520	MMT/Hecto
040168	12:27:10.792	47:11:22.92	0.206	0.632	16.550	MMT/Hecto
040169	10:49:29.349	58:45:59.01	0.421	0.788	8.350	MMT/Hecto
040170	12:14:21.256	47:50:39.52	0.190	3.676	21.880	MMT/Hecto
040176	12:20:58.375	45:56:04.84	0.348	0.455	11.590	MMT/Hecto
040313	12:16:25.161	48:21:56.79	0.266	1.481	7.600	MMT/Hecto
040316	14:11:23.433	52:26:04.15	0.443	1.471	11.610	MMT/Hecto
040318	14:17:19.807	53:06:45.00	0.300	0.646	12.360	MMT/Hecto
040343	10:39:09.748	58:40:39.15	0.343	0.628	5.380	MMT/Hecto
040377	10:40:51.832	58:52:53.22	0.352	0.643	15.250	MMT/Hecto
040434	12:21:24.595	45:53:41.62	0.654	1.559	4.260	MMT/Hecto
040473	10:58:22.401	58:29:00.95	0.161	2.872	17.760	MMT/Hecto
040477	16:20:33.996	54:48:24.00	0.346	0.888	11.110	MMT/Hecto

Notes.

^a Separation of the SN from the center of its host galaxy, normalized by the size and orientation of the host (the R parameter; Sullivan et al. 2006). The isophotal radius of a galaxy corresponds to $R \simeq 3$.

^b The Tonry & Davis (1979) cross-correlation parameter, computed by comparing the host galaxy spectrum to a template spectrum to determine the host redshift. Redshifts with $R > 4$ are treated as reliable in this work, though 1.4% of all redshifts are expected to be spurious, as discussed in J17.

(This table is available in its entirety in machine-readable form.)

With these data, we measure cosmological parameters from 1169 PS1 SNe and 195 low- z SNe Ia in two steps: (1) marginalizing over CC SNe and reducing the data to a set of distance measurements at 25 redshifts (log-spaced in the range $0.01 < z < 0.7$) and (2) using those distances, redshifts, uncertainties, and covariances to infer cosmological parameters with the cosmological Monte Carlo software (CosmoMC; Lewis & Bridle 2002). CosmoMC allows us to easily include the latest CMB, BAO, and/or H_0 priors in our cosmological

constraints. This two-step procedure is similar to that of B14 (see their Appendix E).

3.1. The Likelihood Model

The SN likelihood model used here is discussed and tested comprehensively in J17 and is based on the BEAMS algorithm presented in Kunz et al. (2007).²¹ We summarize the model below.

²¹ Our code is available online at <https://github.com/djones1040/BEAMS>.

Table 4
Free Parameters in the Likelihood Model

	N_{params}	Prior	Comments
$f(z_{b,\text{Ia}})$	25	...	z -dependent model of SN Ia corrected magnitudes
$g(z_{b,\text{CC}})$	5	$2 \pm 3 + (\mu_{\Lambda\text{CDM}}(z_{b,\text{CC}}) - \mathcal{M})$	z -dependent model of CC SN corrected magnitudes
Σ_{Ia}	1	0.1 ± 0.1	SN Ia dispersion
$\Sigma_{\text{CC}}(z_{b,\text{CC}})$	5	2 ± 2	CC SN dispersion
Δ_M	1	0.07 ± 0.07	Host mass step
α	1	0.155 ± 0.05	SALT2 nuisance parameter α
β	1	2.947 ± 0.50	SALT2 nuisance parameter β
A	1	1.0 ± 0.2	Renormalization parameter for P(Ia)
S	1	0.0 ± 0.2	Shift parameter for P(Ia)

Note. List of free parameters and their priors in the BEAMS likelihood model. Here $z_{b,\text{Ia}}$ denotes redshift control points for the SN Ia model, and $z_{b,\text{CC}}$ denotes redshift control points for the CC SN model. The central values of the α and β priors are the best-fit values using PS1 spectroscopically confirmed SNe Ia alone.

To measure distances from SNe Ia, we sample a posterior distribution $P(\theta|D)$ that is proportional to a set of priors $P(\theta)$ and the product (over N SNe) of the likelihoods of the model given the data for each individual SN. Here D is the data, while θ is the set of free parameters in the model. The specific free parameters comprising θ are discussed in the paragraphs below and summarized in Table 4.

We use a three-Gaussian form of the SN likelihood, \mathcal{L} . The SNe Ia are represented by two Gaussians: one for SNe Ia in low-mass hosts, $\mathcal{L}_i^{\text{Ia},M<10}$, and one for SNe Ia in high-mass hosts, $\mathcal{L}_i^{\text{Ia},M>10}$. The CC SNe are represented by the third Gaussian, $\mathcal{L}_i^{\text{CC}}$ (alternative CC SN models are given in Section 4.5),

$$\begin{aligned}
P(\theta|D) &\propto P(\theta) \times \prod_{i=1}^N (\mathcal{L}_i^{\text{Ia},M<10} + \mathcal{L}_i^{\text{Ia},M>10} + \mathcal{L}_i^{\text{CC}}), \\
\mathcal{L}_i^{\text{Ia},M<10} &= \frac{P_i(M < 10)P_i(\text{Ia})}{\sqrt{2\pi(\sigma_{i,\text{Ia}}^2 + \Sigma_{\text{Ia}}^2)}} \\
&\quad \times \exp\left[-\frac{(m_{i,\text{Ia}}^{\text{corr}} + \Delta_M - f(z_i))^2}{2(\sigma_{i,\text{Ia}}^2 + \Sigma_{\text{Ia}}^2)}\right], \\
\mathcal{L}_i^{\text{Ia},M>10} &= \frac{P_i(M > 10)P_i(\text{Ia})}{\sqrt{2\pi(\sigma_{i,\text{Ia}}^2 + \Sigma_{\text{Ia}}^2)}} \\
&\quad \times \exp\left[-\frac{(m_{i,\text{Ia}}^{\text{corr}} - f(z_i))^2}{2(\sigma_{i,\text{Ia}}^2 + \Sigma_{\text{Ia}}^2)}\right], \\
\mathcal{L}_i^{\text{CC}} &= \frac{P_i(\text{CC})}{\sqrt{2\pi(\sigma_{i,\text{CC}}^2 + \Sigma_{\text{CC}}(z_i)^2)}} \\
&\quad \times \exp\left[-\frac{(m_{i,\text{CC}}^{\text{corr}} - g(z_i))^2}{2(\sigma_{i,\text{CC}}^2 + \Sigma_{\text{CC}}(z_i)^2)}\right]. \tag{3}
\end{aligned}$$

Here $m_{i,\text{Ia}}^{\text{corr}}$ and $m_{i,\text{CC}}^{\text{corr}}$ (in the exponential terms) are shape- and color-corrected magnitudes for the i th SN that we compute from the SALT2 parameters m_B , x_1 , c , and Δ_B using the Tripp estimator. They are functions of nuisance parameters α and β (Equation (1); $m_{i,\text{Ia}}^{\text{corr}} = \mu_i + \mathcal{M}$). Because we only wish to measure SALT2 nuisance parameters from SNe Ia, we allow separate values of α and β in the Ia and CC components of the likelihood. The $m_{i,\text{Ia}}^{\text{corr}}$ values are computed using free parameters α_{Ia} and β_{Ia} . The $m_{i,\text{CC}}^{\text{corr}}$ values use α_{CC} and β_{CC} ,

which are fixed to the values for SNe Ia given by B14 (allowing these to be free parameters does not improve the cosmological results). The parameters $\sigma_{i,\text{Ia}}$ and $\sigma_{i,\text{CC}}$ are the uncertainties on the corrected magnitudes of the i th SN using $(\alpha_{\text{Ia}}, \beta_{\text{Ia}})$ or $(\alpha_{\text{CC}}, \beta_{\text{CC}})$, respectively.

The mass step, Δ_M , is a free parameter that adjusts the $m_{i,\text{Ia}}^{\text{corr}}$ of SNe Ia in low-mass hosts to match those in high-mass hosts. In the $\mathcal{L}_i^{\text{Ia},M<10}$ and $\mathcal{L}_i^{\text{Ia},M>10}$ terms in Equation (3), $P_i(M > 10)$ and $P_i(M < 10) = 1 - P_i(M > 10)$ are the probabilities from host masses and host mass measurement uncertainties that a given SN has a host galaxy with mass >10 or <10 dex, respectively. We treat the uncertainties as Gaussian, an approximation that predominantly affects only the minority ($\sim 25\%$) of SNe that have host masses within 1σ of $\log(M_*/M_\odot) = 10$. In previous cosmological analyses (e.g., B14), the uncertainties on $\log(M_*/M_\odot)$ were neglected.

If the SN host galaxy has been misidentified, this could contribute to the systematic uncertainties on cosmological parameters. But for the photometrically classified sample, misidentified host galaxies would have incorrect redshifts and are therefore treated as part of the contaminating distribution ($\mathcal{L}_i^{\text{CC}}$). They then contribute to the ‘‘contamination’’ systematic, as discussed in J17. For spectroscopically classified SNe without host galaxy redshifts, we expect only ~ 2 SNe Ia to have misidentified host galaxies (based on the $1.2\% \pm 0.5\%$ fraction of mismatched host galaxies computed in J17).

The variable of interest for cosmological parameter estimation is $f(z_i)$. It is the continuous, z -dependent model for the SN Ia corrected magnitudes—the mean of the SN Ia Gaussian—and is allowed to vary across the redshift range of the survey ($0.01 < z < 0.7$). We evaluate the model at any z across this redshift range by choosing a fixed set of 25 log-spaced redshift ‘‘control points’’ (z_b ; $\Delta \log_{10}(z) = 0.077$) at which the corrected SN Ia magnitudes $f(z_b) = \mu(z_b) + \mathcal{M}$ are free parameters. For any redshift z_i , we interpolate between the redshift control points below (z_b) and above (z_{b+1}),

$$\begin{aligned}
\mu(z_i) &= (1 - \xi)\mu_b + \xi\mu_{b+1} \\
\xi &= \log(z_i/z_b) / \log(z_{b+1}/z_b), \tag{4}
\end{aligned}$$

where μ_b is the distance modulus at redshift z_b . Interpolating with a simple linear model instead of Λ CDM produces differences of <1 mmag at all redshifts. The SN Ia dispersion

Σ_{Ia} plays the same role as the intrinsic dispersion and is kept fixed at all redshifts.

The z -dependent mean and standard deviation of the CC SN Gaussian model ($g(z_i)$ and $\Sigma_{\text{CC}}(z_i)$) are interpolated between five log-spaced redshift control points. Unlike SNe Ia, the dispersion of the heterogeneous CC SN population changes with redshift due to strong detection biases at high z .

Each Gaussian is multiplied by the prior probability ($P_i(\text{Ia})$ and $P_i(\text{CC}) = 1 - P_i(\text{Ia})$) that a given SN is or is not of Type Ia. We use the PSNID classifier to estimate these probabilities. Alternative classification methods are included as part of our systematic error budget (Section 4.5).

For SNe with photometric classifications, our method allows the type priors to be shifted and renormalized to account for incorrect classifications (see J17). For spectroscopically classified SNe Ia, we set the prior probabilities, $P_i(\text{Ia})$, equal to 1 and do not allow them to be adjusted. We include broad Gaussian priors (Table 4) on all free parameters with the exception of $f(z_b)$, the SN Ia corrected magnitudes. We apply no priors (i.e., flat priors) to $f(z_b)$ to avoid any possibility of cosmological bias.

We estimate the free parameters by sampling the log of the posterior with a Markov chain Monte Carlo (MCMC) algorithm. As in J17, we use the Parallel-Tempered Ensemble Sampler from emcee as our MCMC method (Foreman-Mackey et al. 2013).

3.2. Constraining Cosmological Parameters

From the methods presented above, we infer the corrected magnitudes of SNe Ia at 25 redshift control points, $f(z_b)$, using the baseline SN light-curve parameters, bias corrections, and J17 methodology. We also measure the set of $f(z_b)$ for each systematic uncertainty (Section 4). From these values, a systematic error covariance matrix C_{sys} is created (Conley et al. 2011; Scolnic et al. 2014):

$$C_{\text{sys}}^{jk} = \sum_{n=1}^N \frac{\partial f(z_j)}{\partial S_n} \frac{\partial f(z_k)}{\partial S_n} \sigma(S_n^2). \quad (5)$$

The sum is over all N systematics, and $\frac{\partial f(z_j)}{\partial S_n}$ is the change in corrected magnitude after applying a single systematic S_n to the individual light curves. Here $\sigma(S_n)$ is the size of each systematic uncertainty. The systematic covariance matrix is then combined with the statistical covariance matrix:

$$C_{\text{tot}} = D_{\text{stat}} + C_{\text{sys}}. \quad (6)$$

Note that the statistics-only covariance matrix, D_{stat} , includes both diagonal and off-diagonal components because the magnitudes $f(z_b)$ are anticorrelated with the neighboring magnitudes $f(z_{b+1})$ and $f(z_{b-1})$:

$$D_{\text{stat}}^{ij} = \sum_k^{N_{\text{MCMC}}} \frac{(f_k(z_{b,i}) - \overline{f(z_{b,i})})(f_k(z_{b,j}) - \overline{f(z_{b,j})})}{N_{\text{MCMC}}}. \quad (7)$$

Here N_{MCMC} is the length of the MCMC chain that samples free parameters $f(z_b)$, $f_k(z_{b,i})$ is the value of f at the i th control point from the k th MCMC sample, and $\overline{f(z_{b,i})}$ is the mean of f

at the i th control point from the full MCMC chain. Figure 6 shows the reduced correlation matrices from statistical uncertainties alone (left) and statistical and systematic uncertainties combined (right). The statistics-only correlation matrix shows significant anticorrelations between neighboring control points, while the systematic uncertainties add larger-scale correlations between the control points (see Figure 7).

We then use the CosmoMC software (Lewis & Bridle 2002) to measure cosmological parameters by minimizing the following χ^2 :

$$\chi^2 = (\mu'(z_b) - \mu_{\Lambda\text{CDM}}(z_b; \Omega_M, w, \dots))^{\dagger} C_{\text{tot}}^{-1} \times (\mu'(z_b) - \mu_{\Lambda\text{CDM}}(z_b; \Omega_M, w, \dots)), \quad (8)$$

where $\mu'(z_b) = f(z_b) - \mathcal{M}$ (we marginalize over \mathcal{M} using CosmoMC). The vector of model distances, $\mu_{\Lambda\text{CDM}} = 5 \log(d_L) - 5$, is a function of the cosmology:

$$d_L(z, w, \Omega_M, \Omega_{\Lambda}, \Omega_K) = (1+z) \frac{c}{H_0} \int_0^z \frac{dz}{E(z)},$$

$$E(z) = [\Omega_M(1+z)^3 + \Omega_K(1+z)^2 + \Omega_{\Lambda}(1+z)^{3(1+w)}]^{1/2}. \quad (9)$$

The parameter Ω_M is the cosmic matter density, Ω_{Λ} is the dark energy density, Ω_K is the curvature of space, and w is the redshift-independent dark energy equation-of-state parameter (z dependence will be added in Section 6).

4. Systematic Uncertainties

The SNe in this sample are affected by systematic uncertainties that can broadly be attributed to eight sources of error: Milky Way extinction, distance bias correction, photometric calibration, SALT2 model calibration, sample contamination (primarily by CC SNe), low- z peculiar-velocity corrections, the redshift dependence of SN nuisance parameters, and the dependence of SN Ia luminosities on their host galaxies. Figure 7 illustrates the redshift dependence of each type of systematic uncertainty. We discuss each of these uncertainties in detail below.

4.1. Milky Way Extinction

Milky Way extinctions for each SN are given by Schlafly & Finkbeiner (2011), who used the colors of stars with spectra in SDSS to derive a 14% correction to the reddening maps of Schlegel et al. (1998). We assume a conservative, fully correlated 5% uncertainty on the $E(B-V)$ measurements of Schlafly & Finkbeiner (2011), which could be caused by selection biases in the SDSS stars chosen for spectroscopic follow-up or the use of stars that lie in front of some fraction of the Galactic dust (Schlafly & Finkbeiner 2011).

4.2. Distance Bias Correction

Two effects lead to systematic uncertainties in distance bias corrections. The dominant effect is the difference between the G10 and C11 distance bias predictions. As discussed in Section 2.3.2, the difference between the G10 and C11 dispersion models is up to $\Delta\mu(z) \sim 0.03$ mag. As there is no a priori reason to choose one dispersion model over the other,

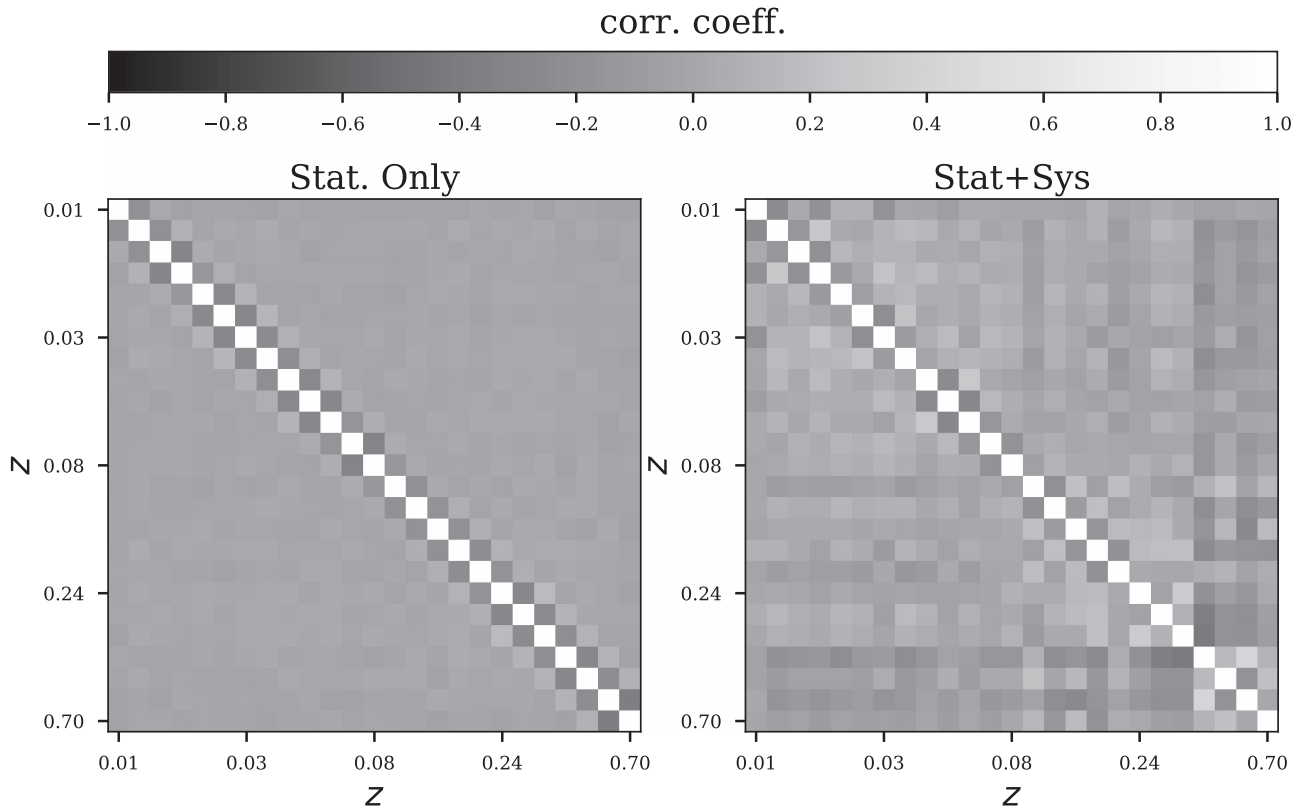


Figure 6. Statistics-only and stat+sys correlation matrices from the PS1+low- z SN sample. The statistics-only correlation matrix shows the strong anticorrelation between neighboring bins. The stat+sys correlation matrix shows larger-scale correlations due to systematic uncertainties and large uncertainties in the bins with minimal data ($z \sim 0.1$ – 0.2). The correlation matrix is equal to $C_{ij}/\sqrt{C_{ii}C_{jj}}$ for covariance matrix C .

we choose to adopt the average of the two bias predictions for our baseline distance bias correction. The systematic error then becomes half the difference between the G10/C11 bias.

A secondary effect is that uncertainty in the survey detection limit or spectroscopic follow-up selection function can cause the simulated distance bias to be inaccurate. We adjust the detection efficiency (for the PS1 host- z sample) and the spectroscopic selection efficiency (for the PS1 SN- z sample) such that the S/N at maximum light for simulated SNe matches the data with an $\sim 20\%$ higher reduced χ^2 (a 1σ difference). These efficiencies are well-constrained by the data; the detection efficiency adjustment for the host- z sample, for example, corresponds to lowering the magnitude limit of the survey by ~ 4 mmag.

The low- z distance bias is measured from low- z simulations that lack reliable detection and spectroscopic selection efficiencies. For these simulations, we use the “volume-limited” simulations discussed in Section 2.3.1 as the selection bias systematic. The volume-limited variant has <0.01 mag distance bias using the G10 scatter model (small biases due to the correlation of Hubble residuals with x_1 and c still arise; Scolnic & Kessler 2016) and a bias of ~ 0.02 mag using the C11 model because $\beta_{\text{fit}} - \beta_{\text{sim}} = 0.7$. The systematic uncertainty due to the detection limit and spectroscopic follow-up selection function is subdominant to the G10/C11 systematic uncertainty.

4.3. Photometric Calibration Uncertainties

In this work, the systematic uncertainties in the photometric calibration are the same as those in the S17 analysis. They are

due to uncertainties in the survey filter functions, calibration of *HST* CALSPEC standard stars, and calibration of the PS1/low- z photometric systems relative to *HST*.

Uncertainties in the survey filter functions are modeled as uncertainties in the zero points and effective wavelengths of each filter. PS1 has a effective central wavelength uncertainty of 7 \AA per filter (Scolnic et al. 2015). The low- z filter uncertainties are typically ~ 6 – 7 \AA but are survey- and filter-dependent. They can be as high as 25 – 37 \AA (exact values are given in Scolnic et al. 2015; see their Table 1).

The relative calibration uncertainties are given by the Supercal method. Supercal uses the excellent (sub-1%) relative calibration of PS1 across 3π sr to compare the photometry of tertiary standard stars in previous SN surveys to the photometry of these same stars on the PS1 system. Typical corrections are on the order of 1% but can be up to 2.5% for B -band low- z data. Uncertainties in the Supercal procedure are typically 3–4 mmag per filter but can be up to 10 mmag for low- z surveys such as CfA1.

Finally, there is uncertainty in the AB magnitude system itself, as measured using *HST* CALSPEC standard stars. We follow B14 by assuming a global 0.5% slope uncertainty for the flux as a function of wavelength, which was determined by comparing white dwarf models to the *HST* data (Betoule et al. 2013; Bohlin 2014). In total, we include 62 individual systematic uncertainties to describe the uncertainty in the photometric calibration. Most are due to the relative calibration: there is one systematic for the filter zero point and the filter $\lambda_{\text{eff}} \times$ number of surveys \times number of filters per survey.

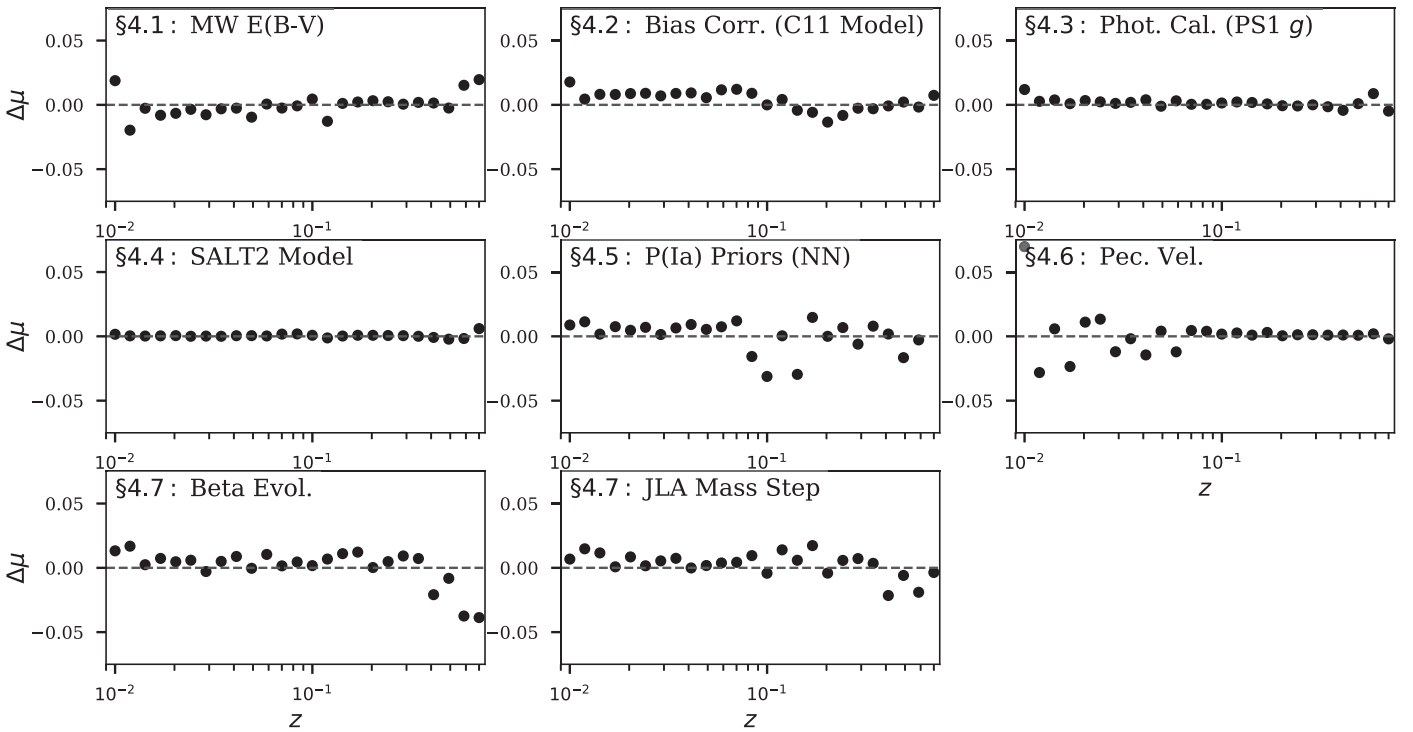


Figure 7. Average change in distance modulus $\Delta\mu$ from an example of each type of systematic uncertainty in this analysis. Deviations at $z \simeq 0.01$ and $\simeq 0.1$ are primarily due to low SN statistics in these bins and have little effect on the cosmological constraints.

4.4. SALT2 Model Calibration Uncertainties

The training of the SALT2 model is subject to the same sources of photometric calibration uncertainty discussed above. B14 created variants of the SALT2.4 light-curve model by applying zero-point and filter function shifts to the training data and subsequently retraining SALT2. These account for 10 individual systematics, which are averaged to give the SALT2 model systematic error. These uncertainties are discussed in Section 5.4 of B14.

Retraining SALT2 using the improved calibration from Supercal will lower the SALT2 systematic uncertainty in future analyses. However, we do not retrain the SALT2 light-curve model for this analysis, as the SALT2 training data are not public.

4.5. CC SN Contamination

Systematic error due to marginalizing over the contamination in our sample is a new source of uncertainty caused by our use of photometrically classified SNe. J17 predicted that the PS1 host- z sample contains $\sim 9\%$ CC SNe. Our method of measuring distances from SNe Ia while marginalizing over CC SNe is subject to biases in two areas: inaccurate prior probabilities that a given SN is of Type Ia and differences between the CC SN model and the true distribution of CC SNe. The systematic error estimation from CC SN contamination was presented in detail in J17 and relies on varying these components.

We use the four methods of estimating prior probability discussed previously (Section 2.4) and three parametric models for the CC SN distribution. The baseline likelihood model for CC SNe, $\mathcal{L}_i^{\text{CC}}$ (Equation (3)), is a Gaussian with a mean and standard deviation— $g(z_i)$ and $\Sigma_{\text{CC}}(z_i)$ for the i th SN—that are both functions of redshift. The two alternate CC SN parametric models are a two-Gaussian model and a skewed Gaussian model. We demonstrated in J17 that these models typically

agree well with single-Gaussian results; all three CC SN distributions tend to be much broader than the SN Ia distribution, therefore encompassing most outliers regardless of whether the functional form is an exact representation of the CC SN data.

Because several of these variants are highly covariant with one another, we group the different contamination variants into two systematics: one using the results from SN classifiers trained on simulated CC SN data and a second using “untrained” classifiers. The trained classifiers include NN and PSNID. The trained systematic is the average change in SN distances when either the NN or PSNID classifier is used with alternate CC SN models. *Fitprob* and *GalSNID* are not trained on simulations, and so we include the average of the *Fitprob* and *GalSNID* distances as a second systematic. The untrained classifiers are not optimal methods but are included here as an alternative to classifiers that depend on simulations with limited CC SN templates and known biases. If each variant were instead treated as an individual systematic, our final uncertainty would only increase by 2%, and the final value of w would be higher by just 0.003.

Finally, we found in J17 that BEAMS can yield results with less bias if α and β are fixed to their known values from spectroscopically classified samples. For a single-Gaussian CC SN model with PSNID, we include this variant in our systematic uncertainty budget by forcing α and β to be equal to the values measured from spectroscopically confirmed PS1 +low- z SNe. The shape and color distributions in the full PS1 sample are different than those in the PS1 spectroscopically classified sample, which could mean that α and β are in fact not the same in the full sample as in the spectroscopically classified sample (Scolnic & Kessler 2016). However, because it is not possible to distinguish between true differences in α/β and differences caused by the known α/β biases when

marginalizing over CC SNe (J17), this variant is a necessary addition to the error budget.

4.6. Peculiar-velocity Correction

The magnitude of SN peculiar velocities, due to bulk flows and nearby superclusters, becomes $\gtrsim 5\%$ of the Hubble flow at $z \lesssim 0.03$. We correct for peculiar velocities using the nearby galaxy density field measured by the 2M++ catalog from 2MASS (Lavaux & Hudson 2011). The uncorrelated uncertainty associated with each correction is $\pm 250 \text{ km s}^{-1}$ (S17). The peculiar-velocity model is parameterized by the equation $\beta_I = \Omega_M^{0.55} / b_I$, where b_I describes the light-to-matter bias. (The parameter β_I is unrelated to the SALT2 nuisance parameter.) Carrick et al. (2015) measured $\beta_I = 0.43 \pm 0.021$. We adopt a conservative 5σ (± 0.1) systematic on β_I for our peculiar-velocity systematic uncertainty.

4.7. SN Ia Demographic Shifts

Though SNe Ia have been shown to be excellent standardizable candles at low- z , it has been suggested that the relationship between their luminosities, colors, and host galaxy properties may change with redshift. We address these possibilities by adding three systematic tests. For these tests, we add additional parameters to our model for estimating cosmological parameters (Section 3). The first is to allow a linear evolution of the mass step as a function of redshift. Mass step evolution was proposed by Childress et al. (2014) and could be observed if the mass step is caused by physical differences in SNe Ia with different progenitor ages. The second is to allow a linear evolution in the SALT2 color-standardization parameter, β , as a function of redshift. This was suggested as a possible concern by Conley et al. (2011). The third is evolution in SALT2 α . Then, Δ_M , α , and β in Equations (1) and (3) become

$$\begin{aligned} \Delta_M &= \Delta_{M,0} + \Delta_{M,1} \times z, \\ \alpha &= \alpha_0 + \alpha_1 \times z, \\ \beta &= \beta_0 + \beta_1 \times z. \end{aligned} \quad (10)$$

Here $\Delta_{M,0}$, $\Delta_{M,1}$, β_0 , β_1 , α_0 , and α_1 are free parameters. They are measured simultaneously with SN Ia distances in Section 5. Because we find no hint of Mass step evolution or α evolution, we include only β evolution as a systematic uncertainty in our final measurement (see Section 5).

We also include a Δ_M variant that shifts the divide between ‘‘low-mass’’ and ‘‘high-mass’’ hosts by 0.15 dex relative to the standard divide at $\log(M_*/M_\odot) = 10$, following the uncertainty on the location of the step measured by S17. Finally, because possible bias in Δ_M due to marginalizing over CC SN contamination was not estimated in J17, we add one variant where Δ_M is fixed to the value measured by B14 ($0.07 \pm 0.023 \text{ mag}$).

We note that because our sample preferentially contains bright host galaxies, our results are sensitive to uncertainty in the relation between host galaxy properties and SN luminosity. However, because most low- z SNe originate from SN searches that specifically targeted bright galaxies, the PS1 photometric data are in some ways more similar to the existing low- z data than to previous high- z data sets. In this way, our results might be less biased by the uncertainty in the relationships between SNe and their host galaxies than those of previous analyses.

An additional potential systematic is the relation between SN Ia corrected magnitudes and their local host galaxy

environments. Several papers have recently asserted that SN Ia corrected magnitudes are correlated with their local star formation environments on a scale of $\sim 1\text{--}3 \text{ kpc}$ (the LSF step; Rigault et al. 2013, 2015). Due to the $\sim 1''$ PSF of PS1 and the lack of ultraviolet or u -band observations for much of our sample, it is impossible to measure robust local star formation rates over the PS1 redshift range. However, Jones et al. (2015) reexamined the evidence for the LSF step, finding that the retraining of SALT2 in B14/G10 reduced or eliminated many of the biases in the SALT2 model. Jones et al. (2015) found no evidence for an LSF step in the B14 low- z sample. Roman et al. (2017) also recently measured a strong dependence of SN Ia luminosities on local $U - V$ color but found that this effect is expected to change w by just 0.006 relative to the standard Δ_M correction. Though our data are not optimal for investigating local properties, we plan to use PS1 data to more robustly determine the relationship between SNe Ia and their global or semi-local host galaxy properties in future work.

5. First Results and Consistency Checks

The PS1+low- z Hubble diagram is shown in Figure 8, and the light-curve parameters for our full sample are given in Table 2. There are ~ 3.5 times as many photometrically classified SNe as there are spectroscopically classified SNe. The binned SN Ia distance uncertainties from the full sample are an average of 40% lower than those from spectroscopically classified SNe Ia alone (statistical uncertainties only). At $0.2 < z < 0.5$, where $\sim 75\%$ of the PS1 data lie, uncertainties are $\sim 45\%$ lower. This is in spite of the fact that the photometrically classified SNe have a lower average S/N; the median S/N at peak is 22 for all PS1 SNe, compared to 38 for spectroscopically classified SNe. We also do not expect that marginalizing over CC SNe has inflated the binned distance uncertainties. In J17, we used simulated data to find that our method of marginalizing over CC SNe increases the statistical uncertainty on binned SN Ia distances by just 3%.

Our likelihood model (Equation (3)) is simultaneously used to measure α , β , and the dispersion Σ_{Ia} , which are given in Table 5. These measurements use the baseline classification method, PSNID, and the one-Gaussian CC SN model, while the alternate methods contribute to the systematic errors in the middle column. We measure $\alpha = 0.165 \pm 0.019$ (stat+sys), which is consistent with the value measured by S17 from low- z , PS1, SDSS, and SNLS spectroscopically confirmed SNe ($\alpha = 0.156 \pm 0.006$). Zhang et al. (2017) also found $\alpha = 0.165 \pm 0.010$ for low- z SNe. However, we note that this value is higher than that measured by B14 by $\sim 1\sigma$ ($\sim 2.5\sigma$ from statistical uncertainties alone), and the reason for this difference is unclear.

The uncertainty on the SN Ia dispersion, $\Sigma_{\text{Ia}} = 0.082 \pm 0.067$, is extremely high. This is a consequence of removing $P(\text{Ia}) < 0.5$ SNe from the sample before cosmological parameter estimation and allowing SN type probabilities to be shifted and renormalized by the likelihood model. If $P(\text{Ia}) < 0.5$ SNe are included, we find that Σ_{Ia} is better constrained, with a value of 0.106 ± 0.032 (stat. errors only), consistent with $\Sigma_{\text{Ia}} = 0.118$ from spectroscopically classified SNe Ia alone. We note that in spite of the large uncertainty on Σ_{Ia} , the distance uncertainties are slightly smaller when $P(\text{Ia}) < 0.5$ SNe are removed. Removing $P(\text{Ia}) < 0.5$ SNe changes the statistics-only measurement of w by just 0.3%.

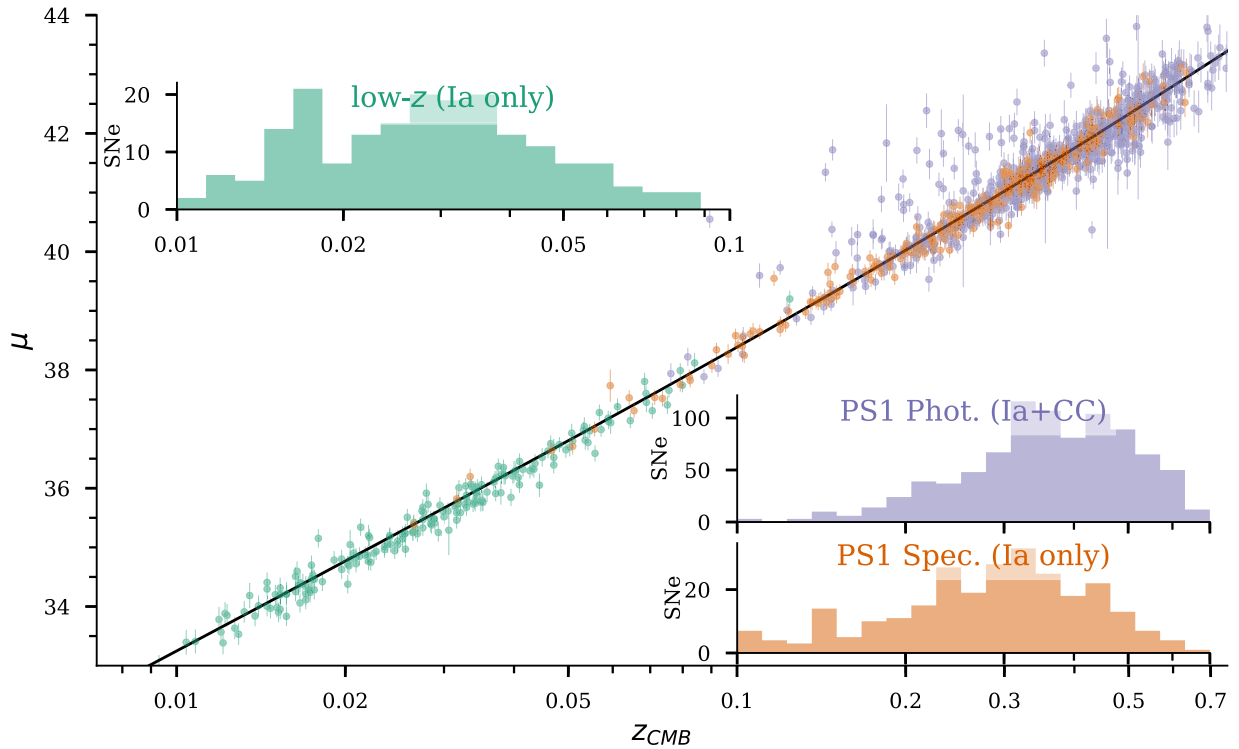


Figure 8. The PS1+low- z Hubble diagram with low- z SNe Ia, spectroscopically classified SNe Ia, and photometrically classified SNe. The data that appear much fainter than Λ CDM (black line) are likely CC SN contaminants. We use 1364 SNe to measure cosmological parameters.

Table 5
Nuisance Parameters

	All SNe		Spec. Class. SNe		
	σ_{stat}	$\sigma_{\text{stat}+\text{sys}}$	σ_{stat}	σ_{stat}	
α	0.165	0.006	0.019	0.155	0.009
β	3.028	0.067	0.152	2.944	0.092
Σ_{Ia}	0.082	0.067	0.101	0.118	0.008
Δ_M	0.102	0.013	0.017 ^a	0.064	0.020

Note. Nuisance parameters from PS1+low- z SNe. The systematic uncertainty on β is likely overestimated due to the biases from the GalSNID and *Fitprob* classification methods discussed in J17. The exceptionally large uncertainty on Σ_{Ia} is due to our decision to exclude SNe with $P(\text{Ia}) < 0.5$ and allow $P(\text{Ia})$ to be shifted and renormalized, but we have verified that this choice has a minimal effect on the final cosmological parameters.

^a The systematic uncertainty excludes the analysis variants that change the location, size, and z dependence of Δ_M .

As a test, if the sample is analyzed without BEAMS, i.e., treating all SNe as SNe Ia, Σ_{Ia} increases by 71% to 0.187. In general, the systematic error on all nuisance parameters is higher than it would be in an analysis of spectroscopically classified SNe Ia, due to the predicted biases on those parameters when marginalizing over CC SN contamination (J17). Fortunately, J17 found that biases of 3%–6% on nuisance parameters do not give similar fractional biases on binned distances or w ($0.5\% \pm 0.4\%$ bias on w for the baseline method).

In J17, we predicted that our method of marginalizing over CC SNe would bias α and β by +3%. This gives a prediction that the α and β measured here will be higher than the α and β measured from spectroscopically confirmed SNe Ia alone. Table 5 shows that this may indeed be the case; α is 6%

higher and β is 3% higher than the values from spectroscopically confirmed PS1+low- z SNe Ia (though at $< 1\sigma$ significance if we neglect the partial correlations between these two samples). However, we also expect higher measured values of β due to the redder colors of the full PS1 sample (Scolnic & Kessler 2016).

We also measure the mass step at 6σ significance and nearly 8σ from statistical errors alone (we report systematic uncertainties that neglect the host mass variants). Our measurement of $\Delta_M = 0.102 \pm 0.017$ is consistent with the B14 measurement of 0.07 ± 0.023 . It is also consistent with the Δ_M that we measure from the low- z sample alone, $\Delta_M = 0.110 \pm 0.038$. Interestingly, the host mass step Δ_M is higher in the full PS1+low- z sample than in the sample of spectroscopically classified SNe Ia alone (1.1σ significance from statistical uncertainties alone, though these measurements are not independent). It is unclear if this difference could be due to statistical fluctuation, a bias from the method, or the presence of broader light-curve shapes and redder colors in the full sample. Because x_1 and c correlate with both the host mass and Hubble residual (Scolnic & Kessler 2016), different x_1 and c distributions could increase the size of the step (S17). We will use simulations to investigate whether our method of marginalizing over CC SN contamination could bias determinations of the host mass step in future work.

5.1. Impact of Different Classification Methods

Regardless of which classifier is used, uncertainties on binned distances from the full PS1 sample are much smaller than the uncertainties on binned distances from spectroscopically classified SNe Ia alone (by $\gtrsim 40\%$). The binned SN Ia distance measurements from each classifier are also remarkably consistent (Figure 9). Nearly all distances are

within 1σ of distances derived from the PS1 spectroscopically classified SN Ia sample. Additionally, binned distances from $0.2 \lesssim z \lesssim 0.5$, where 75% of our data lie, show few discrepancies between the different methods. Even the test case of using an uninformative prior of $P(\text{Ia}) = 1/2$ for all photometrically classified SNe (bottom panel) yields distances within 1σ of the spectroscopic sample in all bins but one. We note that close agreement is predicted by J17; even in a sample without spectroscopically confirmed SNe Ia, J17 predicted biases of <10 mmag due to the method. We will revisit this prediction in Section 8 to test whether our methodology remains robust and consistent in the case of an “ideal” photometrically classified SN sample, i.e., a sample without spectroscopic classifications.

The nuisance parameters α and β , as measured using different classification priors, are more consistent than expected from J17. When using different classification priors, α and β vary by 30%–50% less than the simulation-based predictions in J17 (in this work, we observe differences of $\Delta\beta \sim 0.07$ and $\Delta\alpha \sim 0.004$ between the four different classification methods). In Figure 10, we provide a possible explanation for why our results are more consistent than expected. J17 simulations included no subset of spectroscopically classified PS1 SNe, while our data consist of $\sim 24\%$ spectroscopically classified PS1 SNe. Because of this, we used simulations of the PS1 host- z and SN- z samples (Section 2.3.1) to predict the effect of adding spectroscopically classified subsets of SNe to the data. We find that the predicted biases on α and β due to marginalizing over CC SNe decrease by 30%–40% when the PS1 data consist of 24% spectroscopically classified SNe.

Similarly, the biases on individual distance bins decrease by $\sim 30\%$ – 40% when 24% of PS1 SNe are spectroscopically classified. For PSNID priors, Figure 10 shows that the predicted (weighted) average bias in distance modulus at $z > 0.1$ relative to $z < 0.1$ is just 2 mmag.

5.2. Evolution of Nuisance Parameters

Using Equation (10) to add linear Mass step (Δ_M) evolution to BEAMS, we find no evolution in Δ_M as a function of redshift (we use the baseline classifier, PSNID). However, our uncertainties are large, ~ 0.08 mag, due to a lack of low-mass hosts at high redshift.²² In Figure 11, we estimate the redshift dependence of the mass step with a 2.5σ clip of Hubble residuals ($-0.45 \lesssim \text{HR} \lesssim 0.45$) to remove most CC SNe and then plot the maximum-likelihood mass step in redshift bins of 0.1. This is an incomplete removal of CC SN contamination, but it doubles as a simple sanity check on BEAMS. We find no statistically significant evidence for Mass step evolution.

We do see 1.6σ evidence for evolution of the β parameter, however (Figure 12). Fortunately, this does not constitute a large contribution to our systematic error budget, as it predominantly affects the highest survey redshifts where few SNe are found (Figure 7). Evidence for β evolution was seen in SNLS data (Conley et al. 2011), though its significance is attributed to selection effects in B14. S17 found just 1σ evidence for β evolution ($\beta = (3.139 \pm 0.099) + z \times (-0.348 \pm 0.289)$), a measurement that includes SNe at redshifts up to ~ 2 (Riess et al. 2018). Though there are not enough SNe Ia at $z > 1.5$ to constrain

²² S17, however, found evidence of Mass step evolution. The discrepancy could be due to the larger SNLS redshift range and additional SNe Ia in low-mass hosts at $z > 0.5$.

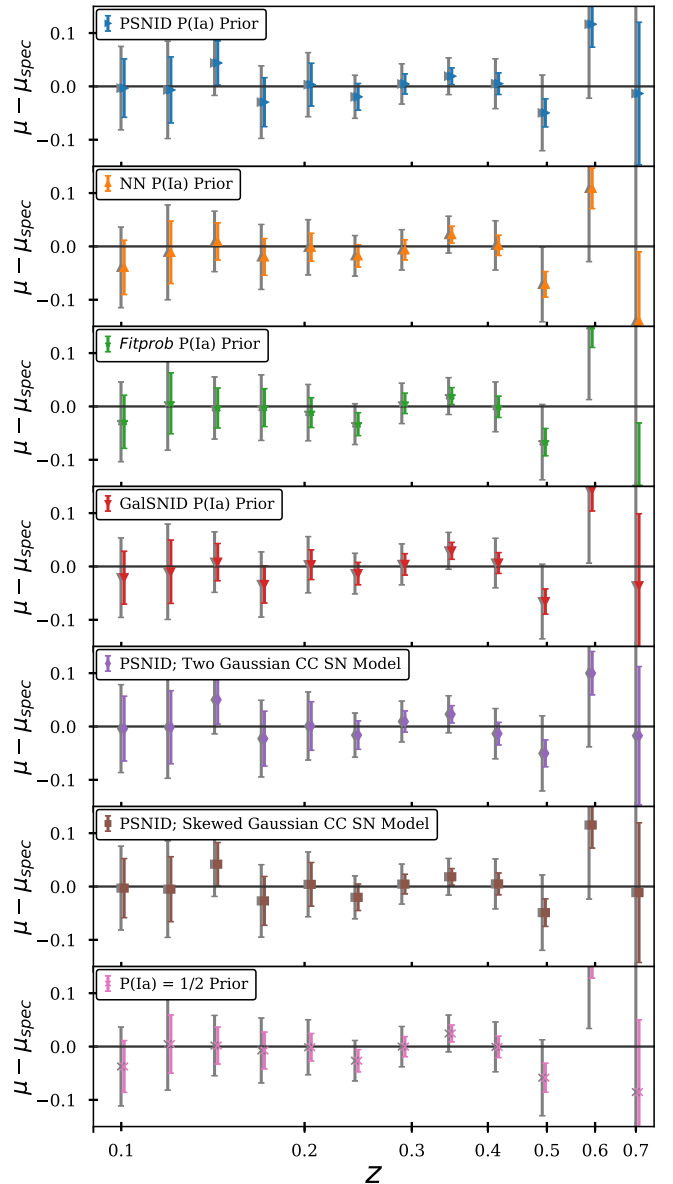


Figure 9. Difference in binned distance from the full photometric sample compared to binned distances from the subset of ~ 280 spectroscopically classified PS1 SNe Ia. Gray (large) error bars are the uncertainties on spectroscopic and photometric distances added in quadrature, while the smaller errors are from the photometric sample alone (small redshift offsets are added to the photometric points for visual clarity). Binned distances are consistent between methods, with a small bump at $z \sim 0.35$ that could be due to high CC SN contamination at this redshift but is also consistent with statistical fluctuation. For comparison to the predicted biases from simulations, see Figure 11 of J17.

a changing value of β , larger high- z data sets may be able to confirm or discount β evolution. We caution that blue ($c < 0$) SNe Ia have lower observed β (SNe primarily appear blue due to noise and selection biases; Scolnic & Kessler 2016), and our high- z data are dominated by blue SNe (Figure 1). However, our methodology does not recover any significant evolution of β when tested on simulated SN samples with a constant input β . In 10 simulated SN samples, five using the G10 model and five using the C11 model, we found just a single sample showing $>1\sigma$ evidence of negative β evolution with redshift (the simulation had a β slope with significance of 1.2σ). If β does change with z , it could suggest an evolution in dust properties or the evolution of

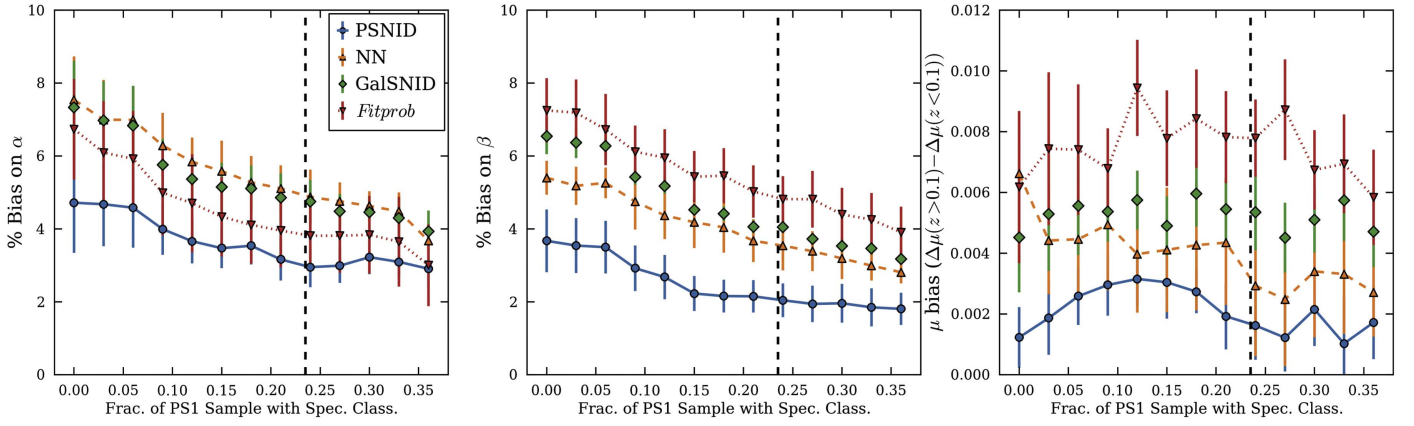


Figure 10. From simulations, the bias on α , β , and distance due to marginalizing over CC SNe as a function of the fraction of spectroscopically classified SNe Ia in the data. In this work, $\sim 24\%$ of the PS1 sample is spectroscopically classified (vertical lines), giving a predicted reduction in α/β bias of $\sim 30\%$ – 40% . The typical reduction in bias for a single distance bin is also $\sim 30\%$ – 40% , although the average distance bias at $z > 0.1$ relative to $z < 0.1$ is largely unchanged (within the errors) with additional spectroscopic classifications.

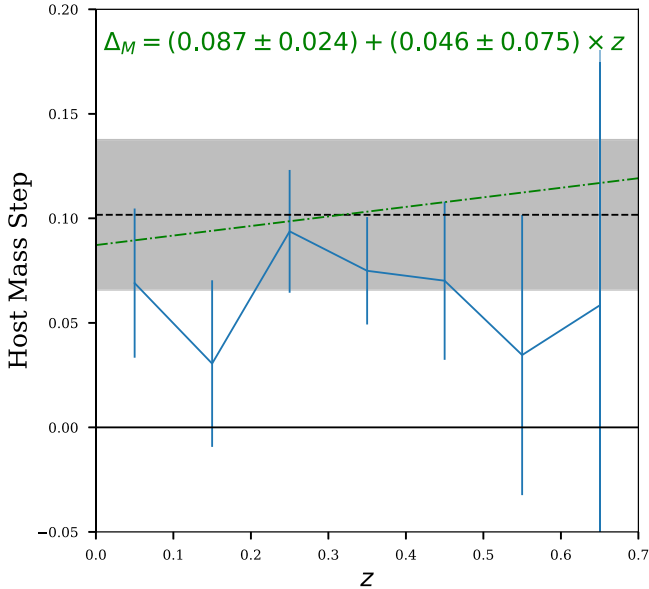


Figure 11. Evolution of the host galaxy mass step with redshift after 2.5σ clipping to remove most CC SNe. Binned points are shown with the best-fit global mass step (black) and linear trend (green) from marginalizing over CC SNe.

SN progenitors with redshift and could contribute significantly to the systematic error budget at $z > 0.5$.

We also checked for α evolution using the same parametric form as Equation (10) and find $\alpha(z) = 0.157 \pm 0.01 + z * (0.018 + / - 0.040)$. Because we find that α evolution is not statistically significant, we have not included it in our systematic uncertainty budget.

6. Cosmological Constraints from SN and CMB Data

We first constrain Ω_M using the SN Ia data alone and assuming a flat Λ CDM cosmology. We find $\Omega_M = 0.319 \pm 0.040$, consistent with B14 (0.295 ± 0.034). These results are independent of but in good agreement with the Planck constraints on Ω_M ($\Omega_M = 0.308 \pm 0.012$).

We combine these data with CMB constraints from the Planck full-mission data (Planck Collaboration et al. 2016a). In contrast to the Planck Collaboration et al. (2014) constraints used in B14, the full-mission Planck data do not require WMAP polarization measurements. Planck provides the full likelihoods

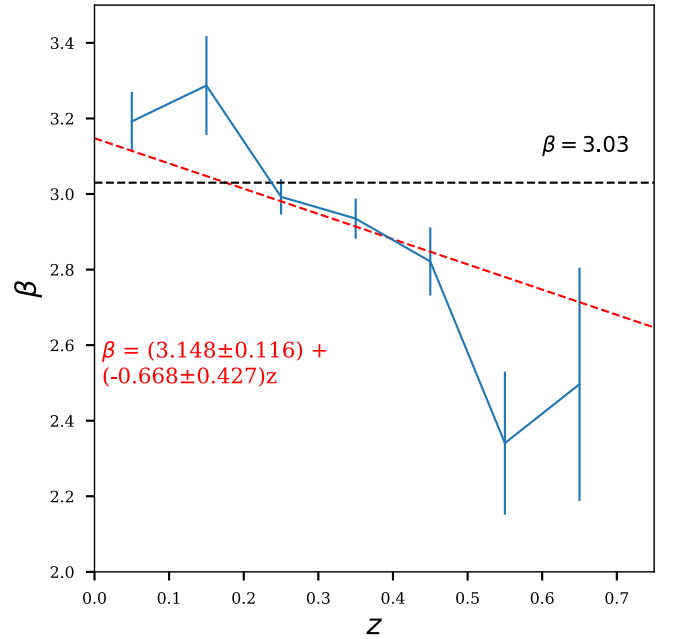


Figure 12. Binned evolution of the SALT2 nuisance parameter β with redshift after 2.5σ clipping to remove most CC SNe. The best-fit β (black) and linear trend (red) are computed by marginalizing over CC SNe with the full-likelihood model.

for the CMB data, which can then be combined with SNe Ia using CosmoMC. Planck data greatly improve our constraints on w using the CMB temperature power spectrum, which gives a precise constraint on the cosmic matter density at $z \sim 1090$. Constraints from a matter-dominated cosmic epoch are largely independent of an evolving or noncosmological constant dark energy, which affects cosmic evolution only at the late times probed by SN Ia and BAO measurements.

With Planck priors, we measure $w = -0.989 \pm 0.057$ (stat +sys). Systematic uncertainties on this measurement are 14% higher than statistical uncertainties (Table 6). Though we have 85% more SNe than B14 and 31% more SNe than S17, our uncertainty is approximately the same as B14 and 39% higher than S17. There are three primary reasons for this. First, we have fewer independent surveys to reduce the photometric calibration systematic. Second, we have estimated a more conservative systematic uncertainty on the selection bias

Table 6
Summary of Systematic Uncertainties on w

Error	Δw^a	$\Delta \sigma_w^b$	Rel. to σ_w^{stat}
All sys.	0.033	0.043	1.137
Phot. cal.	0.007	0.021	0.558
Bias corr.	0.012	0.019	0.518
Mass step	0.006	0.017	0.449
Beta evol.	0.012	0.016	0.428
MW $E(B-V)$	0.009	0.015	0.390
CC SN contam.	-0.001	0.012	0.332
SALT2 model	0.001	0.008	0.207
Pec. vel.	0.002	0.007	0.182

Notes.

^a Difference in measured w relative to the final value of w with all systematics included.

^b The additional uncertainty added in quadrature from each source of systematic error. The statistical uncertainty on w is 0.0375.

correction than B14. Lastly, PS1 photometrically classified SNe have much lower S/Ns (for PS1, the S/N at maximum is an average of 17 for photometrically classified SNe and 39 for spectroscopically classified SNe Ia), and PS1 SNe, unlike SNLS SNe, cannot be found at $z \sim 0.7-1$.

We also use these data to constrain the two-parameter redshift evolution of w using the most common parameterization:

$$w = w_0 + w_a z / (1 + z). \quad (11)$$

Equation (11) is a first-order Taylor series expansion of w as a function of scale factor a (Linder 2003). We find $w_0 = -0.912 \pm 0.149$ and $w_a = -0.513 \pm 0.826$. These constraints are slightly better than those of B14, which is due to our use of the most recent chains from Planck. We also find much tighter constraints on w_a after combining with BAO (Section 7).

6.1. Systematic Uncertainties on w

Contributions to the systematic uncertainties on w are summarized in Table 6. The photometric calibration systematic, the largest source of systematic uncertainty in most previous analyses (e.g., R14, B14), remains the largest systematic uncertainty in this work ($\sigma_w^{\text{cal}} = 0.021$) but is now almost the same magnitude as the selection bias. The calibration has been significantly improved by the Supercal procedure, and continued improvements will come from a new network of white dwarf standards (Narayan et al. 2016).

The second-largest systematic uncertainty is due to the selection bias ($\sigma_w^{\text{bias}} = 0.020$). The σ_w^{bias} is dominated by the difference between the G10 and C11 scatter models and the uncertain spectroscopic selection function of the low- z surveys. It may be that retraining SALT2 assuming the C11 scatter model, e.g., Mosher et al. (2014), will reduce this systematic in the future.

The systematic due to marginalizing over CC SNe, $\sigma_w^{\text{CC}} = 0.012$, is the third-smallest systematic, nearly equal in size to the Milky Way extinction systematic and smaller than the systematics pertaining to the host mass step and β evolution. Table 7 shows the value of w measured from each classification prior and CC SN parameterization discussed in Section 4. All measurements of w are within 2% of the baseline method. We note that it is likely that the NN and PSNID classifiers are more accurate than the other two classifiers used in this work. However, both NN and PSNID are directly dependent on CC SN templates and simulations for training,

Table 7
 w with Different Photometric Classification Priors and CC SN Models

Method	Δw	$\Delta \sigma_w$
PSNID
PSNID, skewed Gaussian CC model	-0.004	0.000
PSNID, 2-Gaussian CC model	0.018	0.011
NN	0.016	0.000
GalSNID	0.008	0.000
Fitprob	-0.007	0.000
Spec. α/β	-0.008	0.000

Note. The w from each CC SN model and photometric classification prior, relative to the baseline case of using PSNID classification priors and a single, z -dependent Gaussian to model the CC SNe. The final line is the change in w when α and β are fixed to the values measured from spectroscopically confirmed SNe Ia.

neither of which are likely representative of the true CC SN population (see J17 for more discussion). We include the alternative *Fitprob* and GalSNID classifiers, as they are less subject to the uncertainty in CC SN simulations, but we note that excluding them would significantly reduce the systematic uncertainty due to CC SN contamination.

The dispersion of measured w from different BEAMS variants is nearly $\sim 25\%$ lower than predicted by J17, in spite of the fact that, unlike J17, we did not fix α and β to the values from the spectroscopic sample (except for the final variant listed in Table 7). This may be due to sample-to-sample variations but is more likely explained by tighter constraints on Ω_M from the full Planck chains compared to the J17 approximation (Ω_M prior of 0.30 ± 0.02) and the fact that a sizable portion ($\sim 24\%$) of our high- z data are spectroscopically classified SNe Ia. With simulations, we found that a subset of SNe with known types can greatly help the BEAMS method to constrain distances and SN Ia nuisance parameters (Section 5). If the amount of CC SN contamination was overestimated in J17, that could also help to explain the lower contamination systematic. The magnitude of the CC SN contamination systematic can be further reduced by improved validation of classifiers and a better understanding of the diversity of CC SNe and their luminosity functions, as well as the inclusion of additional CC SN templates in classifier training, as discussed in J17. Methods for measuring robust classifications, even in the case where the training sample is biased (e.g., Revsbech et al. 2018), are also important to pursue.

7. Cosmological Constraints with BAO and H_0 Priors

We now combine Planck (Planck Collaboration et al. 2016a) and PS1+low- z SNe with BAO constraints and a local prior on the value of H_0 from Riess et al. (2016). The BAO feature, the evolving size of the imprint of acoustic waves on the distribution of cosmic matter, serves as a standard ruler that is independent of SN Ia measurements. The BAO scale is proportional to a combination of the angular diameter distance to a given redshift and the Hubble parameter $H(z)$ at that redshift. Following Planck Collaboration et al. (2016a), we use BAO constraints from the SDSS Main Galaxy Sample (MGS; Ross et al. 2015) and the combination of the Baryon Oscillation Spectroscopic Survey (BOSS) and CMASS survey (Anderson et al. 2014). The BAO constraints used here give measurements of the BAO scale to $z = 0.15, 0.32, \text{ and } 0.57$.

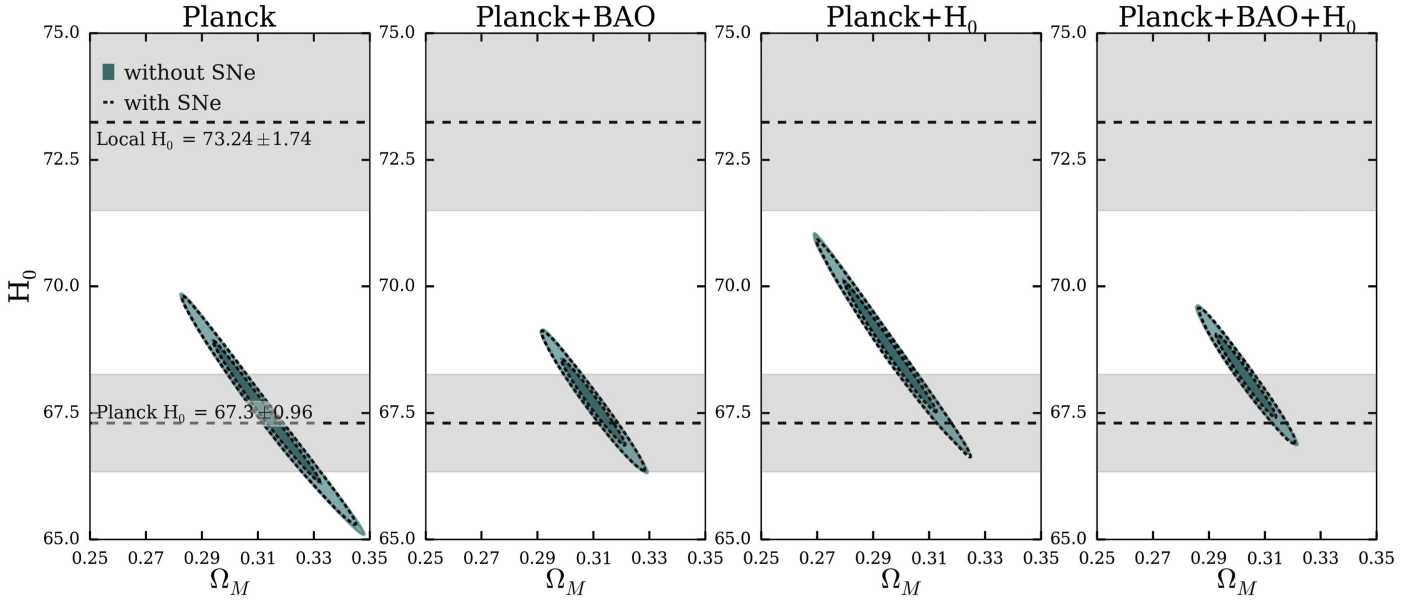


Figure 13. Discrepant constraints on H_0 from CMB, BAO, and local measurements assuming Λ CDM. SNe Ia disfavor a scenario in which exotic dark energy can resolve these conflicts.

Table 8
Cosmological Parameters from PS1, BAO, CMB, and H_0

$\sigma - \Lambda$ CDM Constraints				
	Ω_M	Ω_Λ	Ω_k	H_0
PS1+Planck+BAO+ H_0	0.303 ± 0.007	0.694 ± 0.008	0.003 ± 0.002	68.682 ± 0.694
PS1+Planck	0.330 ± 0.045	0.674 ± 0.035	-0.004 ± 0.011	66.205 ± 4.659
PS1+Planck+BAO	0.310 ± 0.007	0.689 ± 0.008	0.001 ± 0.003	67.892 ± 0.714
PS1+Planck+ H_0	0.272 ± 0.014	0.718 ± 0.012	0.009 ± 0.003	72.522 ± 1.748
w -CDM Constraints				
	Ω_M	w	H_0	
PS1+Planck+BAO+ H_0	0.299 ± 0.008	-1.045 ± 0.045	69.007 ± 0.980	
PS1+Planck	0.317 ± 0.017	-0.989 ± 0.057	67.140 ± 1.664	
PS1+Planck+BAO	0.312 ± 0.010	-0.984 ± 0.048	67.364 ± 1.091	
PS1+Planck+ H_0	0.289 ± 0.012	-1.067 ± 0.046	70.042 ± 1.263	
w_a -CDM Constraints				
	Ω_M	w_0	w_a	H_0
PS1+Planck+BAO+ H_0	0.301 ± 0.009	-0.972 ± 0.102	-0.372 ± 0.452	69.011 ± 0.994
PS1+Planck	0.308 ± 0.026	-0.912 ± 0.149	-0.513 ± 0.826	68.276 ± 2.752
PS1+Planck+BAO	0.314 ± 0.010	-0.920 ± 0.103	-0.313 ± 0.418	67.371 ± 1.117
PS1+Planck+ H_0	0.277 ± 0.012	-0.812 ± 0.104	-1.323 ± 0.493	71.611 ± 1.365

There is a notable internal conflict between these priors: a 3.4σ discrepancy between local and CMB-inferred values of H_0 (Riess et al. 2016; see also Bonvin et al. 2017; Casertano et al. 2017; Jang & Lee 2017). The difference could be due to systematic uncertainties in one or both data sets (e.g., Addison et al. 2016), >3 neutrino species, non- Λ dark energy, or more exotic phenomena. We show this discrepancy in Figure 13 for a standard Λ CDM cosmology (reionization optical depth $\tau = 0.078$; Planck Collaboration et al. 2016b). PS1+low- z SNe cannot explain the disparity and therefore limit the degree to which exotic dark energy can explain the H_0 tension. Throughout this section, we remain agnostic as to the source of the discrepancy and examine cosmological parameters using all probes both individually and in combination.

Following B14, we use SN data to constrain three cosmological models: the σ - Λ CDM model removes the assumption of flatness ($\Omega_k = 0$); the w -CDM model allows a fixed, non-cosmological constant value of w ; and the w_a -CDM model allows w to evolve with redshift. The constraints on these three models are presented in Table 8. All measurements of w and w_a are consistent with Λ CDM (Figures 14 and 15). With SNe+Planck+BAO+ H_0 constraints, we find $w = -1.045 \pm 0.045$ for the w -CDM model and $w_a = -0.372 \pm 0.452$ for the w_a -CDM model (Figure 15). With just SNe, Planck, and BAO data, we find $w = -0.984 \pm 0.048$ for the w -CDM model and $w_a = -0.313 \pm 0.418$ for the w_a -CDM model.

Nearly all measurements of Ω_k are consistent with a flat universe. The lone exception is the combination of SNe, Planck, and H_0 . This

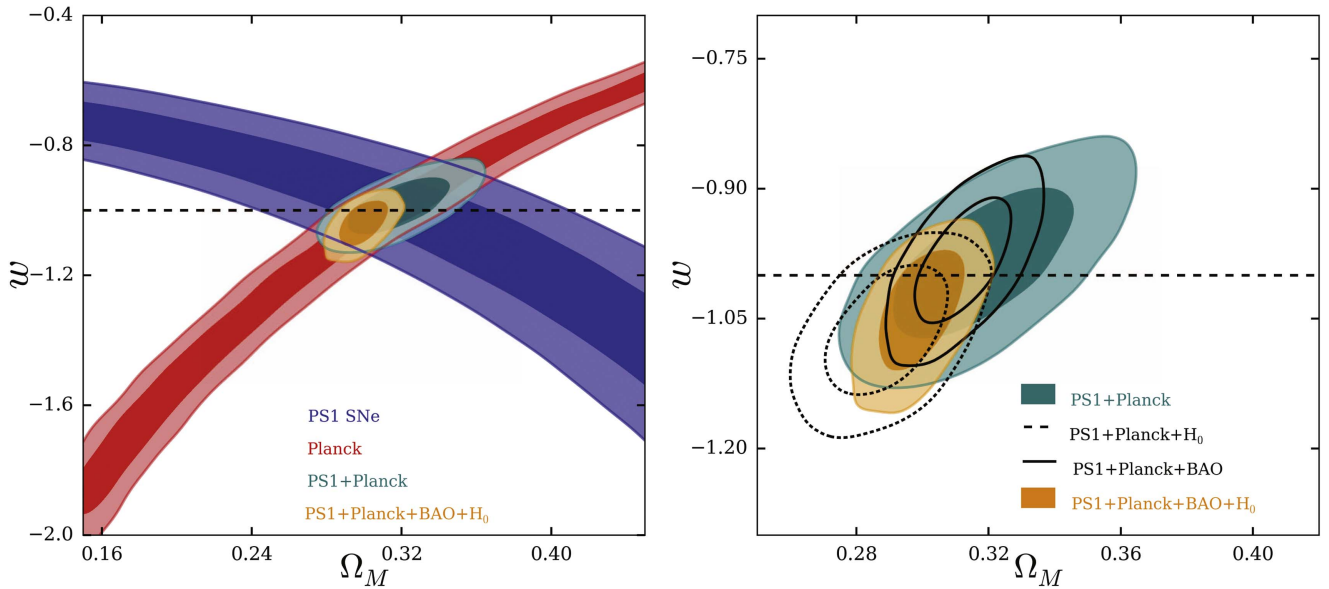


Figure 14. Constraints on w and Ω_M from PS1+low- z SNe in conjunction with other probes.

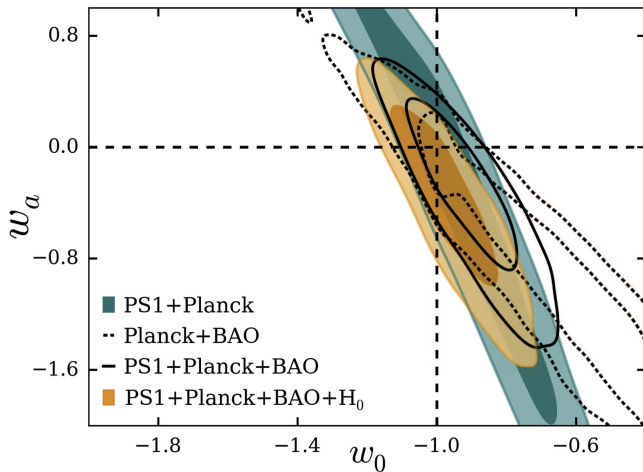


Figure 15. Constraints on w_0 and w_a from PS1+low- z SNe, Planck, BAO, and H_0 .

choice of priors gives 3σ evidence for positive curvature, but the result is entirely due to the local/CMB H_0 discrepancy and becomes insignificant when BAO constraints are added.

As shown from the H_0 measurements in Table 8, PS1+low- z SNe and the non- Λ CDM models considered here do not explain the local/CMB H_0 discrepancy. When H_0 priors are omitted, all measurements of H_0 are inconsistent with Riess et al. (2016) at the $\sim 2\sigma$ – 3σ level and would also be inconsistent with other local measurements of H_0 (Bonvin et al. 2017; Jang & Lee 2017). When only CMB and H_0 priors are included, we measure values of H_0 that are consistent with Riess et al. (2016) only when allowing for positive curvature or evolving w . When we combine with CMB, H_0 , and BAO priors, all measurements of H_0 are inconsistent with Riess et al. (2016) at the 2.6σ – 2.8σ level even though H_0 priors are included. Therefore, SNe Ia and the models considered here do not favor a non- Λ CDM universe or a scenario where the H_0 discrepancy is due to non-cosmological constant dark energy.

7.1. Consistency with JLA and Pantheon Results

The binned SNIa distances from our likelihood model are compared to the JLA sample in Figure 16 (using the correlated bins given by B14, Appendix F). The agreement is close; using weighted average Hubble residuals, PS1+low- z distances are just 4 mmag fainter at $z > 0.2$ compared to $z < 0.2$.

Measurements of w and Ω_M in this work show excellent agreement with B14 and the Pantheon sample (S17). For the flat w -CDM model, Table 9 shows the drift in the values of w we measure with respect to B14 and S17. All values are consistent with B14 values to within 0.4σ . Though these measurements are correlated, as B14 used $\sim 75\%$ of the low- z SNe that we do (with the exception of CfA4 and CSP2), and we combine both SN data sets with the same CMB, BAO, and H_0 data, such close agreement is encouraging.

Similarly, our measurements are consistent with those of S17 at $\lesssim 0.5\sigma$. Though these samples are not entirely independent—34% of the SNe Ia here are included in the Pantheon sample—the samples are subject to different systematic, as well as statistical, uncertainties. The 2% discrepancy between the S17 measurement of w and ours is well within the uncertainty budget of our measurement. In future work, we hope to combine our sample with the Pantheon data, as this combined sample would likely provide the best current constraints on w and include just under 2000 SNe.

Though the results presented here remain subject to uncertainty in the population of CC SNe contaminating the SN data, the agreement with other measurements is encouraging. Our cosmological parameter measurements also remain consistent when using several variants as part of the BEAMS framework. The consistency of these results with measurements from spectroscopically confirmed PS1 SNe determined by S17 ($w = -0.990 \pm 0.063$) gives us additional confidence in their robustness.

In the next few years, we also expect that additional CC SN templates and better constraints on CC SN luminosity functions will lead to even more robust simulation-based tests for this method and other similar methods.

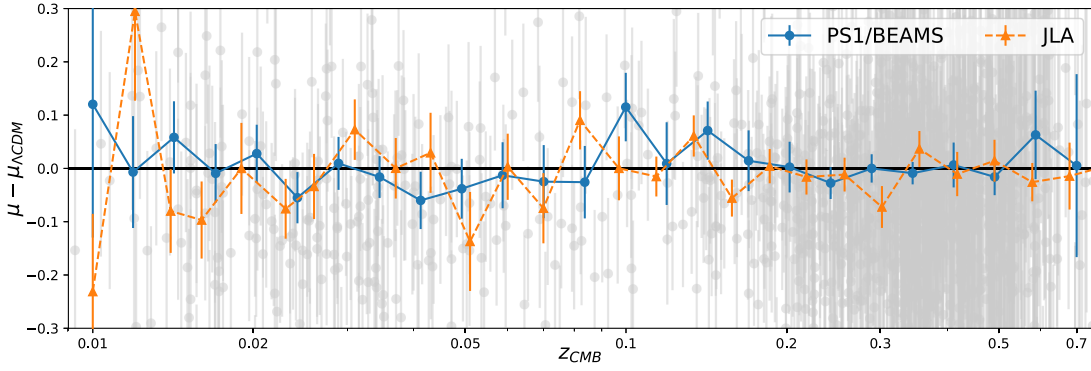


Figure 16. The PS1+low- z Hubble residual diagram, with a comparison to the binned SN Ia distances given by B14. We see excellent agreement with B14 across the redshift range, with slight discrepancies at low- z due to the addition of the CfA4 sample and a stronger prediction for the distance bias correction.

Table 9
Comparison to JLA and Pantheon Cosmological Constraints

	This Work	JLA		Pantheon	
	w	w	Diff.	w	Diff.
SNe+Planck	-0.989 ± 0.057	-1.017 ± 0.056	$0.028 \pm 0.080 (0.35\sigma)$	-1.026 ± 0.041	$0.037 \pm 0.070 (0.52\sigma)$
SNe+Planck+BAO	-0.984 ± 0.048	-1.003 ± 0.047	$0.019 \pm 0.068 (0.28\sigma)$	-1.014 ± 0.040	$0.030 \pm 0.063 (0.48\sigma)$
SNe+Planck+ H_0	-1.067 ± 0.046	-1.064 ± 0.051	$0.010 \pm 0.068 (0.15\sigma)$	-1.056 ± 0.038	$-0.011 \pm 0.060 (0.19\sigma)$
SNe+Planck+BAO+ H_0	-1.045 ± 0.045	-1.038 ± 0.047	$0.012 \pm 0.065 (0.18\sigma)$	-1.047 ± 0.038	$0.002 \pm 0.059 (0.03\sigma)$
	w_a	w_a	Diff.	w_a	Diff.
SNe+Planck	-0.513 ± 0.826	-0.608 ± 0.748	$0.095 \pm 1.115 (0.09\sigma)$	-0.129 ± 0.755	$-0.384 \pm 1.119 (0.34\sigma)$
SNe+Planck+BAO	-0.313 ± 0.418	-0.280 ± 0.433	$-0.033 \pm 0.602 (0.05\sigma)$	-0.126 ± 0.384	$-0.187 \pm 0.567 (0.33\sigma)$
SNe+Planck+ H_0	-1.323 ± 0.493	-1.055 ± 0.586	$-0.168 \pm 0.737 (0.23\sigma)$	-0.742 ± 0.465	$-0.581 \pm 0.678 (0.86\sigma)$
SNe+Planck+BAO+ H_0	-0.372 ± 0.452	-0.290 ± 0.443	$-0.073 \pm 0.648 (0.11\sigma)$	-0.222 ± 0.407	$-0.150 \pm 0.608(0.25\sigma)$

8. Measuring w without Spectroscopic Classifications

Throughout this analysis, we have used spectroscopically confirmed SNe Ia to bolster our cosmological results. However, future samples from DES and LSST may not have a large fraction of spectroscopic classifications. Here we examine distances, nuisance parameters, and measurements of w in the case where no spectroscopic classifications of PS1 SNe are available; we substitute photometric classifications for the available spectroscopic classifications, apply our likelihood model, and measure the resulting bias on w . We investigate the cases of both the full PS1 data set and the host- z sample (only SNe with spectroscopic host galaxy redshifts) to determine whether our methodology can provide consistent results when spectroscopic classifications are lacking. The host- z sample in particular is nearly an ideal, magnitude-limited sample, albeit with host galaxy selection biases. Of SNe in the full PS1 data set, 24% are spectroscopically classified SNe Ia, and 13% of SNe in the host- z sample are spectroscopically classified.

When photometric classifications are used instead of spectroscopic classifications, Figure 17 shows that the binned SN Ia distances may occasionally change by >0.05 mag where statistical uncertainties are large. However, at $0.25 \lesssim z \lesssim 0.5$, where $\sim 75\%$ of our data lie, we see median biases less than 5 mmag for all methods. This is in agreement with predictions from J17, who found that in 25 samples of 1000 high- z SNe, bias due to marginalizing over CC SN contamination averaged <5 mmag and had sample-to-sample variations of ~ 15 mmag in this redshift range. Although here we change at most 24% of the

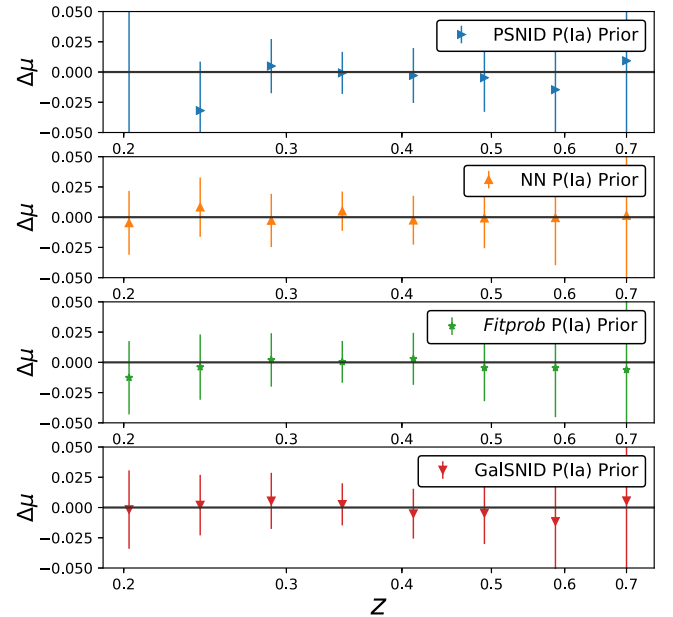


Figure 17. Changes in binned distances when spectroscopic classifications are ignored. Here $\Delta\mu$ is the bias on distance when photometric classifications are used for the $\sim 13\%$ of the sample with spectroscopic classifications available. As we predict in J17, typical biases are <5 mmag for all P(Ia) priors at $0.2 < z < 0.5$ (the average is just 4 mmag for PSNID), with occasionally larger biases in bins with higher statistical uncertainties. PSNID classifies few PS1 SNe at $z < 0.25$ as being likely SNe Ia, and therefore provides no meaningful constraints on distances at these redshifts.

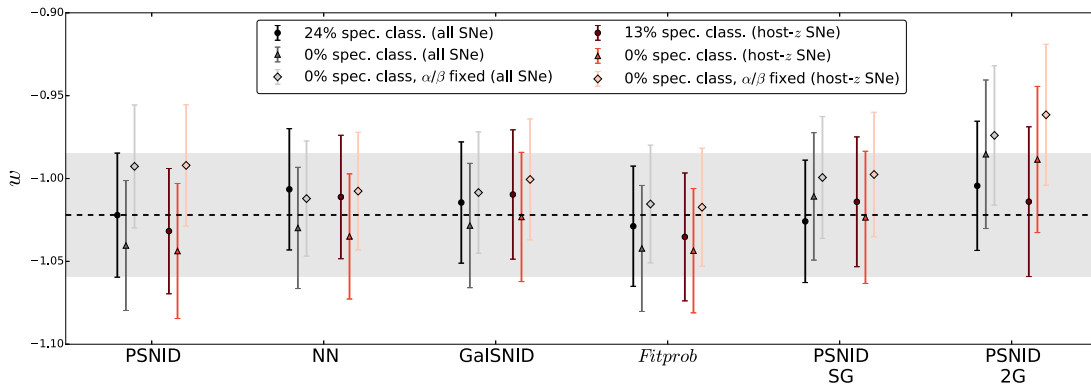


Figure 18. Changes in w if photometric classifications are used instead of the available spectroscopic classifications. The final, statistics-only measurement from PS1 +Planck of $w = -1.022 \pm 0.037$ is shown with the dashed line and light shaded region. We also show the results if α and β remain fixed to the values measured from spectroscopically classified PS1 SNe (points with light shading; α and β are 0.155 and 2.95, respectively). We find that biases of up to $\sim 4\%$ can arise when spectroscopic classifications are not available but are typically ameliorated by fixing α and β to the values measured from spectroscopic samples.

classifications in the sample, the results remain broadly consistent with simulations.

In Figure 18, we examine the change in measured w if spectroscopic classifications are not used. From every classifier, in both the full and host- z samples, we measure a w consistent with the statistical uncertainties on our best measurement of w , $\sigma_w = 0.037$ (and w derived from the host- z sample prefers a value of -1.032 , 1% lower than the full sample due to statistical fluctuations alone). However, the bias in w can be nearly $\sim 4\%$ for the least informative classifiers in this analysis (*Fitprob* and *GalSNID*), which constitutes a strong argument for including a subset of spectroscopic classifications when measuring w or fixing α and β to the values measured from spectroscopic samples—in this case, from PS1 spectroscopically confirmed SNe. Fixing α and β can often improve the reliability of a method, an effect we show in Figure 18.

It is reassuring that many of our results appear to confirm what we predicted using simulations in J17. We see likely negative biases on w when using the *GalSNID* and *Fitprob* classifiers and (typically) more consistent results after fixing α and β . We predicted distance biases at $0.2 < z < 0.5$ of $\lesssim 15$ mmag in a given SN sample, and our results here are consistent with that finding. Though not statistically significant, the \sim few percent differences in nuisance parameters between spectroscopically classified SNe alone and the full sample are in the direction we would expect. With the advent of more robust classifiers and better training samples, we expect the systematic uncertainties to decrease and the reliability of simulations to improve. Even with some modest discrepancies, we see that the consistency level for nearly all methods is well within the uncertainty budget on w , demonstrating a promising future for SN cosmology with photometrically classified SNe.

9. Conclusions

The 1364 cosmologically useful, likely SNe Ia from the PS1 medium-deep fields and low- z surveys constitute the largest set of SNe Ia assembled to date. Our cosmological measurement uncertainties are almost identical to those of the JLA compilation, due to the smaller redshift range and lower S/N of the SNe Ia in our sample, but the measurements presented here are independent of the JLA data at $z > 0.1$. In the future, these data can be used in conjunction with the Foundation low- z SN sample (Foley et al. 2018) to give independent constraints on w using only the well-calibrated PS1 photometric system.

The SN light curves, host galaxy spectra, and host galaxy redshifts presented in this work are available at <https://doi.org/10.17909/T95Q4X>.

The PS1 SNe in this sample do not have spectroscopic classifications, necessitating a Bayesian framework that marginalizes over the CC SN population. By applying this framework, we compute binned distances from SNe Ia that are an average of just 4 mmag fainter at $z > 0.2$, compared to $z < 0.2$, than JLA distances. From J17, we found that this method of marginalizing over CC SNe in a PS1-like sample will bias w by a statistically insignificant 0.001 ± 0.004 .

From these data, we find that shape- and color-corrected SNe Ia in host galaxies with $M_*/M_\odot > 10$ dex are 0.102 ± 0.017 mag (stat+sys) brighter, on average, than those in $M_*/M_\odot < 10$ dex hosts, consistent with previous measurements. We find no evidence for evolution of the mass step with redshift (e.g., Childress et al. 2014) but $\sim 1.6\sigma$ evidence for evolution in the SALT2 β parameter (the correlation between SN color and luminosity).

After including CMB data, we find that PS1 SN data are fully consistent with a flat Λ CDM cosmology, with $w = -0.989 \pm 0.057$. Combining SNe with CMB and BAO constraints gives $w = -0.984 \pm 0.048$, and adding H_0 constraints yields $w = -1.045 \pm 0.045$. If we allow w to be parameterized by a constant component (w_0) and a component that evolves with redshift (w_a), we find no evidence for a z -dependent value of w . Our constraints differ from those of B14 by $< 0.4\sigma$, regardless of whether CMB, BAO, and/or H_0 priors are included. They are also consistent with the constraints from Scolnic et al. (2017).

CC SN contamination is the third-smallest systematic uncertainty in this analysis and can be improved further with new SN classification algorithms and better training samples, as discussed in J17. In future work, our dominant systematics—selection biases and calibration—can be reduced by combining PS1 data with Foundation and/or SNLS and SDSS data.

In carrying out this analysis, we note that we did not blind ourselves to the cosmological results. A blinded analysis, such as that of S17, would remove any subconscious bias on the part of the authors to achieve agreement (or disagreement) with Λ CDM cosmology. We note, however, that all of the photometry and most of the bias-correction simulations were undertaken before the cosmological results were examined. Furthermore, we have strived for consistency with previous analyses whenever possible, which serves to limit the number of qualitative choices that can be tuned to yield a preferred cosmology. Future analyses, such as DES SN Ia cosmology, will be fully blinded. As cosmology with

photometrically classified SNe Ia becomes a more mature subject area, the authors will feel more comfortable undertaking blinded analyses.

In future years, SN samples from the DES and LSST will measure w with larger, higher-S/N samples of SNe without spectroscopic classifications. Though CC SN contamination is the second-largest source of systematic uncertainty on w in this analysis, we expect that the systematic uncertainty on w from CC SN contamination will be greatly reduced in the next few years. Improvements will be due to larger samples of CC SN templates that can be used to train SN classification algorithms and a better understanding of the shape of the CC SN luminosity function. We hope that the methods presented here will demonstrate the robustness of measuring w from photometrically classified samples as we continue to gain a better understanding of the nature of dark energy.

We would like to thank the referee for many insightful comments, which were helpful in improving this manuscript. We would also like to thank Scott Fleming and the Space Telescope Science Institute for their invaluable assistance in making the data presented in this work publicly available and user-friendly. Michael Foley also had many useful suggestions that improved this analysis.

DOJ is supported by a Gordon and Betty Moore Foundation postdoctoral fellowship at the University of California, Santa Cruz. This manuscript is based upon work supported by the National Aeronautics and Space Administration under contract No. NNG16PJ34C issued through the *WFIRST* Science Investigation Teams program. RJF and DS were supported in part by NASA grant 14-WPS14-0048. The UCSC group is supported in part by NSF grant AST-1518052 and by fellowships from the Alfred P. Sloan Foundation and the David and Lucile Packard Foundation to RJF. This work was supported in part by the Kavli Institute for Cosmological Physics at the University of Chicago through grant NSF PHY-1125897 and an endowment from the Kavli Foundation and its founder, Fred Kavli. DS gratefully acknowledges support from NASA grant 14-WPS14-0048. DS is supported by NASA through Hubble Fellowship grant *HST*-HF2-51383.001, awarded by the Space Telescope Science Institute, which is operated by the Association of Universities for Research in Astronomy, Inc., for NASA under contract NAS 5-26555.

Many of the observations reported here were obtained at the MMT Observatory, a joint facility of the Smithsonian Institution and the University of Arizona. This paper uses data products produced by the OIR Telescope Data Center, supported by the Smithsonian Astrophysical Observatory. Additional data are thanks to the Anglo-Australian Telescope, operated by the Australian Astronomical Observatory, through the National Optical Astronomy Observatory (NOAO PropID: 2014B-N0336; PI: D. Jones). We also used data from observations at Kitt Peak National Observatory, National Optical Astronomy Observatory, which is operated by the Association of Universities for Research in Astronomy (AURA) under a cooperative agreement with the National Science Foundation. Also based on observations obtained with the Apache Point Observatory 3.5 m telescope, which is owned and operated by the Astrophysical Research Consortium.

The computations in this paper used a combination of three computing clusters. BEAMS analysis was performed using the University of Chicago Research Computing Center and the

Odyssey cluster at Harvard University. We are grateful for the support of the University of Chicago Research Computing Center for assistance with the calculations carried out in this work. The Odyssey cluster is supported by the FAS Division of Science, Research Computing Group, at Harvard University. Supernova light-curve reprocessing would not have been possible without the Data-Scope project at the Institute for Data Intensive Engineering and Science at Johns Hopkins University.

Funding for the Sloan Digital Sky Survey IV has been provided by the Alfred P. Sloan Foundation, the U.S. Department of Energy Office of Science, and the Participating Institutions. SDSS-IV acknowledges support and resources from the Center for High-Performance Computing at the University of Utah. The SDSS website is <http://www.sdss.org>.

SDSS-IV is managed by the Astrophysical Research Consortium for the Participating Institutions of the SDSS Collaboration, including the Brazilian Participation Group, the Carnegie Institution for Science, Carnegie Mellon University, the Chilean Participation Group, the French Participation Group, the Harvard-Smithsonian Center for Astrophysics, Instituto de Astrofísica de Canarias, the Johns Hopkins University, the Kavli Institute for the Physics and Mathematics of the Universe (IPMU)/University of Tokyo, Lawrence Berkeley National Laboratory, Leibniz Institut für Astrophysik Potsdam (AIP), Max-Planck-Institut für Astronomie (MPIA Heidelberg), Max-Planck-Institut für Astrophysik (MPA Garching), Max-Planck-Institut für Extraterrestrische Physik (MPE), the National Astronomical Observatory of China, New Mexico State University, New York University, the University of Notre Dame, Observatório Nacional/MCTI, the Ohio State University, Pennsylvania State University, the Shanghai Astronomical Observatory, the United Kingdom Participation Group, Universidad Nacional Autónoma de México, the University of Arizona, the University of Colorado–Boulder, the University of Oxford, the University of Portsmouth, the University of Utah, the University of Virginia, the University of Washington, the University of Wisconsin, Vanderbilt University, and Yale University.

This research makes use of the VIPERS-MLS database, operated at CeSAM/LAM, Marseille, France. This work is based in part on observations obtained with WIRCam, a joint project of CFHT, Taiwan, Korea, Canada, and France. The CFHT is operated by the National Research Council (NRC) of Canada, the Institut National des Science de l'Univers of the Centre National de la Recherche Scientifique (CNRS) of France, and the University of Hawaii. This work is based in part on observations made with the *Galaxy Evolution Explorer* (*GALEX*). *GALEX* is a NASA Small Explorer whose mission was developed in cooperation with the Centre National d'Etudes Spatiales (CNES) of France and the Korean Ministry of Science and Technology. *GALEX* is operated for NASA by the California Institute of Technology under NASA contract NAS 5-98034. This work is based in part on data products produced at TERAPIX, available at the Canadian Astronomy Data Centre as part of the Canada–France–Hawaii Telescope Legacy Survey, a collaborative project of NRC and CNRS. The TERAPIX team has performed the reduction of all the WIRCam images and the preparation of the catalogs matched with the T0007 CFHTLS data release.

Funding for the DEEP2 Galaxy Redshift Survey has been provided by NSF grants AST-95-09298, AST-0071048, AST-0507428, and AST-0507483, as well as NASA LTSA grant NNG04GC89G. This research uses data from the VIMOS VLT Deep Survey, obtained from the VVDS database operated by Cesam, Laboratoire d’Astrophysique de Marseille, France. The zCosmos data are based on observations made with ESO telescopes at the La Silla or Paranal Observatories under program ID 175.A-0839.

Appendix Simulating Evolving x_1 and c Distributions

In this appendix, we discuss the improvement to the PS1 simulations by allowing the mean simulated x_1 and c to evolve with redshift. We consider the standard approach of fixed x_1 and c populations insufficient for our analysis, because the PS1 host- z sample has redshift-dependent host galaxy properties due to our magnitude-limited host galaxy redshift follow-up program.

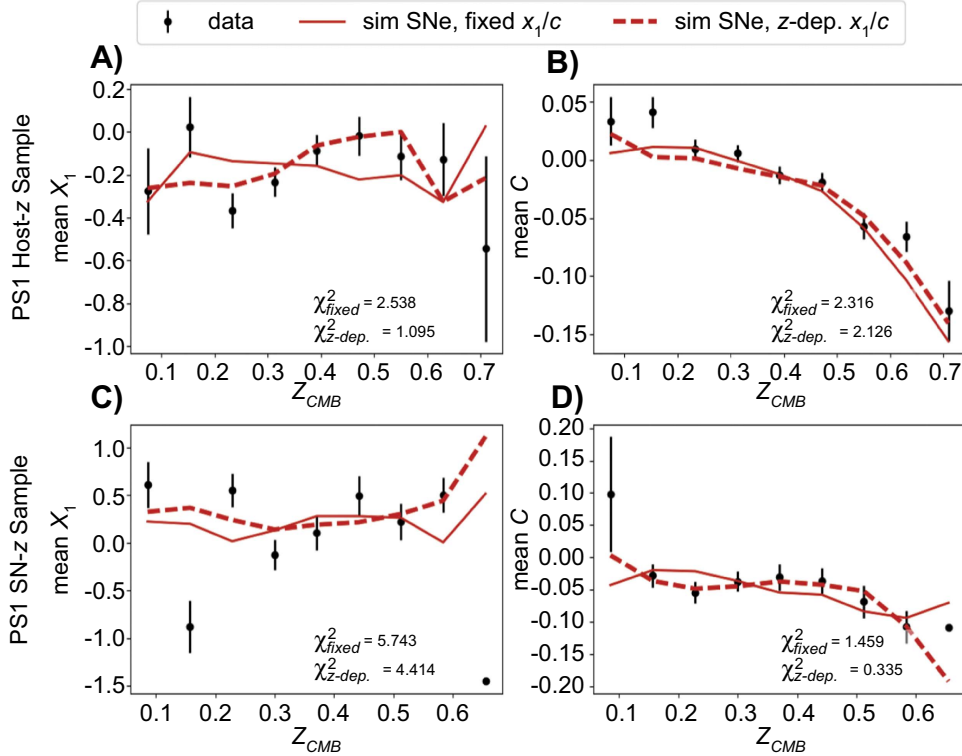


Figure 19. The z dependence of x_1 and c . Allowing x_1 and c to evolve with redshift allows simulations to better match the data.

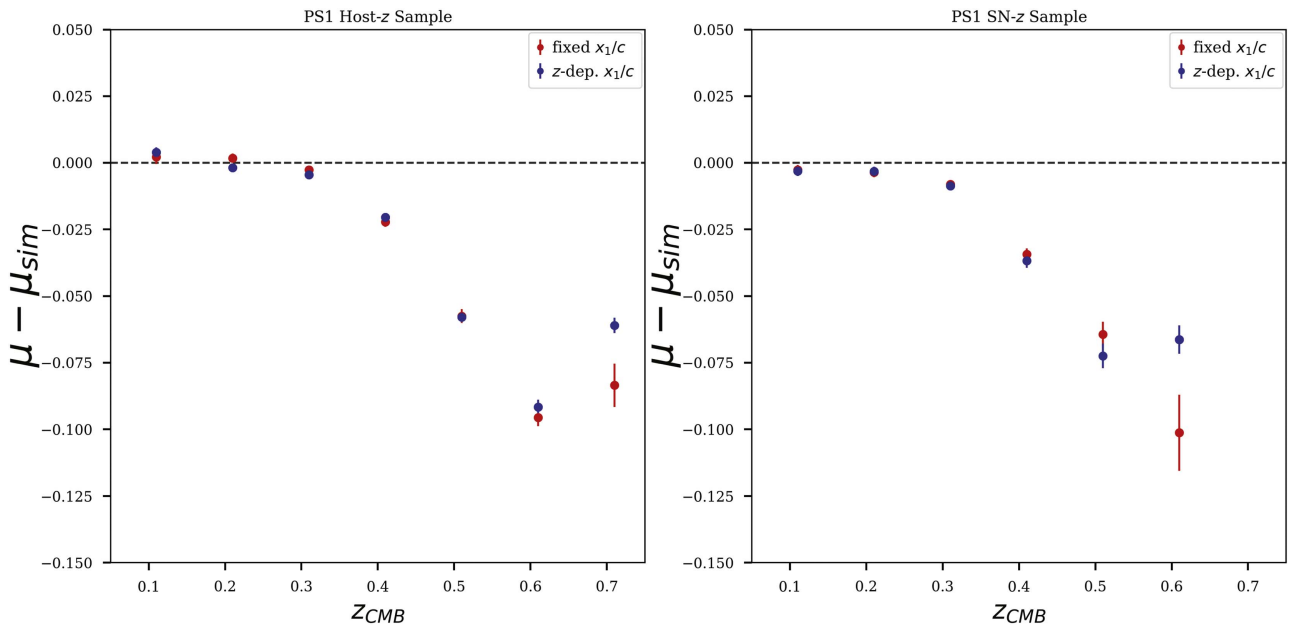


Figure 20. Change in distance bias when simulating x_1/c distributions that evolve with redshift (G10 model). The new simulations can affect the distance bias by ~ 0.01 – 0.02 mag at high z .






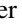
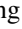








Similarly, the SN- z sample consists of SNe not included in the host- z sample and therefore also has a z -dependent bias. Because x_1 and c depend on host mass, their distributions change as a function of z in a way that is not due only to selection biases.

Using the default simulations for the host- z and SN- z samples from J17 and S17, respectively, we fit a third-order polynomial to the difference between the simulations and the data after binning in redshift ($\Delta z = 0.05$). We used these polynomials as inputs to SNANA, allowing them to define the intrinsic evolution of x_1 and c with redshift.

Figure 19 shows the redshift dependence of the x_1 and c distributions in simulations with fixed and evolving x_1/c . Though allowing x_1 and c to evolve with redshift does improve the simulations, these new simulations are only a moderately better match to the data.

Figure 20 shows the difference in bias corrections using the G10 scatter model with and without z -dependent x_1 and c populations. If x_1 and c are redshift-dependent, the distance bias is slightly larger for the host- z sample and smaller by up to 0.02 mag at high z for the SN- z sample.

ORCID iDs

D. O. Jones  <https://orcid.org/0000-0002-6230-0151>
 E. Berger  <https://orcid.org/0000-0002-9392-9681>
 R. Kessler  <https://orcid.org/0000-0003-3221-0419>
 W. S. Burgett  <https://orcid.org/0000-0003-4401-9582>
 K. C. Chambers  <https://orcid.org/0000-0001-6965-7789>
 P. W. Draper  <https://orcid.org/0000-0002-7204-9802>
 H. Flewelling  <https://orcid.org/0000-0002-1050-4056>
 M. E. Huber  <https://orcid.org/0000-0003-1059-9603>
 N. Kaiser  <https://orcid.org/0000-0001-6511-4306>
 N. Metcalfe  <https://orcid.org/0000-0001-9034-4402>
 J. Tonry  <https://orcid.org/0000-0003-2858-9657>
 R. J. Wainscoat  <https://orcid.org/0000-0002-1341-0952>
 C. Waters  <https://orcid.org/0000-0003-1989-4879>
 R. Kotak  <https://orcid.org/0000-0001-5455-3653>
 S. J. Smartt  <https://orcid.org/0000-0002-8229-1731>

References

- Addison, G. E., Huang, Y., Watts, D. J., et al. 2016, *ApJ*, 818, 132
 Alam, S., Albareti, F. D., Allende Prieto, C., et al. 2015, *ApJS*, 219, 12
 Amendola, L., Appleby, S., Bacon, D., et al. 2013, *LRR*, 16, 6
 Anderson, L., Aubourg, É., Bailey, S., et al. 2014, *MNRAS*, 441, 24
 Astier, P., Guy, J., Regnault, N., et al. 2006, *A&A*, 447, 31
 Bennett, C. L., Halpern, M., Hinshaw, G., et al. 2003, *ApJS*, 148, 1
 Bertin, E., & Arnouts, S. 1996, *A&AS*, 117, 393
 Betoule, M., Kessler, R., Guy, J., et al. 2014, *A&A*, 568, A22
 Betoule, M., Marnier, J., Regnault, N., et al. 2013, *A&A*, 552, A124
 Blake, C., Brough, S., Couch, W., et al. 2008, *A&G*, 49, 5.19
 Bohlin, R. C. 2014, arXiv:1403.6861
 Bonvin, V., Courbin, F., Suyu, S. H., et al. 2017, *MNRAS*, 465, 4914
 Campbell, H., D'Andrea, C. B., Nichol, R. C., et al. 2013, *ApJ*, 763, 88
 Campbell, H., Fraser, M., & Gilmore, G. 2016, *MNRAS*, 457, 3470
 Carrick, J., Turnbull, S. J., Lavaux, G., & Hudson, M. J. 2015, *MNRAS*, 450, 317
 Casertano, S., Riess, A. G., Bucciarelli, B., & Lattanzi, M. G. 2017, *A&A*, 599, A67
 Chambers, K. C., Magnier, E. A., Metcalfe, N., et al. 2016, arXiv:1612.0556
 Childress, M., Aldering, G., Antilogus, P., et al. 2013, *ApJ*, 770, 108
 Childress, M. J., Wolf, C., & Zahid, H. J. 2014, *MNRAS*, 445, 1898
 Chotard, N., Gangler, E., Aldering, G., et al. 2011, *A&A*, 529, L4
 Colless, M., Peterson, B. A., Jackson, C., et al. 2003, arXiv:astro-ph/0306581
 Conley, A., Guy, J., Sullivan, M., et al. 2011, *ApJS*, 192, 1
 Contreras, C., Hamuy, M., Phillips, M. M., et al. 2010, *AJ*, 139, 519
 Dai, M., & Wang, Y. 2016, *MNRAS*, 459, 1819
 Eisenstein, D. J., Zehavi, I., Hogg, D. W., et al. 2005, *ApJ*, 633, 560
 Fabricant, D., Fata, R., Roll, J., et al. 2005, *PASP*, 117, 1411
 Fioc, M., & Rocca-Volmerange, B. 1997, *A&A*, 326, 950
 Flaugher, B. 2005, *IJMPA*, 20, 3121
 Folatelli, G., Phillips, M. M., Burns, C. R., et al. 2010, *AJ*, 139, 120
 Foley, R. J., & Mandel, K. 2013, *ApJ*, 778, 167
 Foley, R. J., Scolnic, D. M., Rest, A., et al. 2018, *MNRAS*, 475, 193
 Foreman-Mackey, D., Hogg, D. W., Lang, D., & Goodman, J. 2013, *PASP*, 125, 306
 Guy, J., Astier, P., Baumont, S., et al. 2007, *A&A*, 466, 11
 Guy, J., Sullivan, M., Conley, A., et al. 2010, *A&A*, 523, A7
 Hamuy, M., Phillips, M. M., Suntzeff, N. B., et al. 1996, *AJ*, 112, 2398
 Hicken, M., Challis, P., Jha, S., et al. 2009a, *ApJ*, 700, 331
 Hicken, M., Challis, P., Kirshner, R. P., et al. 2012, *ApJS*, 200, 12
 Hicken, M., Wood-Vasey, W. M., Blondin, S., et al. 2009b, *ApJ*, 700, 1097
 Hlozek, R., Kunz, M., Bassett, B., et al. 2012, *ApJ*, 752, 79
 Jang, I. S., & Lee, M. G. 2017, *ApJ*, 836, 74
 Jha, S., Kirshner, R. P., Challis, P., et al. 2006, *AJ*, 131, 527
 Jones, D. H., Read, M. A., Saunders, W., et al. 2009, *MNRAS*, 399, 683
 Jones, D. O., Riess, A. G., & Scolnic, D. M. 2015, *ApJ*, 812, 31
 Jones, D. O., Scolnic, D. M., Riess, A. G., et al. 2017, *ApJ*, 843, 6
 Jönsson, J., Sullivan, M., Hook, I., et al. 2010, *MNRAS*, 405, 535
 Kaiser, N., Burgett, W., Chambers, K., et al. 2010, *Proc. SPIE*, 7733, 0
 Kelly, P. L., Hicken, M., Burke, D. L., Mandel, K. S., & Kirshner, R. P. 2010, *ApJ*, 715, 743
 Kessler, R., Bassett, B., Belov, P., et al. 2010, *PASP*, 122, 1415
 Kessler, R., Becker, A. C., Cinabro, D., et al. 2009, *ApJS*, 185, 32
 Kessler, R., & Scolnic, D. 2017, *ApJ*, 836, 56
 Knights, M., Bassett, B. A., Varughese, M., et al. 2013, *JCAP*, 1, 039
 Kunz, M., Bassett, B. A., & Hlozek, R. A. 2007, *PhRvD*, 75, 103508
 Lampeitl, H., Smith, M., Nichol, R. C., et al. 2010, *ApJ*, 722, 566
 Lavaux, G., & Hudson, M. J. 2011, *MNRAS*, 416, 2840
 Le Borgne, D., & Rocca-Volmerange, B. 2002, *A&A*, 386, 446
 Le Fèvre, O., Vettolani, G., Garilli, B., et al. 2005, *A&A*, 439, 845
 Lewis, A., & Bridle, S. 2002, *PhRvD*, 66, 103511
 Lilly, S. J., Le Fèvre, O., Renzini, A., et al. 2007, *ApJS*, 172, 70
 Linder, E. V. 2003, *PhRvL*, 90, 091301
 Lochner, M., McEwen, J. D., Peiris, H. V., Lahav, O., & Winter, M. K. 2016, *ApJS*, 225, 31
 Mink, D. J., Wyatt, W. F., Caldwell, N., et al. 2007, in *ASP Conf. Ser.* 376, *Astronomical Data Analysis Software and Systems XVI*, ed. R. A. Shaw, F. Hill, & D. J. Bell (San Francisco, CA: ASP), 249
 Mosher, J., Guy, J., Kessler, R., et al. 2014, *ApJ*, 793, 16
 Narayan, G., Axelrod, T., Holberg, J. B., et al. 2016, *ApJ*, 822, 67
 Newman, J. A., Cooper, M. C., Davis, M., et al. 2013, *ApJS*, 208, 5
 Padmanabhan, N., Schlegel, D. J., Finkbeiner, D. P., et al. 2008, *ApJ*, 674, 1217
 Pan, Y.-C., Sullivan, M., Maguire, K., et al. 2014, *MNRAS*, 438, 1391
 Perlmutter, S., Aldering, G., Goldhaber, G., et al. 1999, *ApJ*, 517, 565
 Planck Collaboration, Ade, P. A. R., Aghanim, N., et al. 2014, *A&A*, 571, A16
 Planck Collaboration, Ade, P. A. R., Aghanim, N., et al. 2016a, *A&A*, 594, 12
 Planck Collaboration, Aghanim, N., Ashdown, M., et al. 2016b, *A&A*, 596, A107
 Rest, A., Scolnic, D., Foley, R. J., et al. 2014, *ApJ*, 795, 44
 Revsbech, E. A., Trotta, R., & van Dyk, D. A. 2018, *MNRAS*, 473, 3969
 Riess, A. G., Filippenko, A. V., Challis, P., et al. 1998, *AJ*, 116, 1009
 Riess, A. G., Kirshner, R. P., Schmidt, B. P., et al. 1999, *ApJ*, 117, 707
 Riess, A. G., Macri, L. M., Hoffmann, S. L., et al. 2016, *ApJ*, 826, 56
 Riess, A. G., Rodney, S. A., Scolnic, D. M., et al. 2018, *ApJ*, 853, 126
 Riess, A. G., Strolger, L.-G., Casertano, S., et al. 2007, *ApJ*, 659, 98
 Riess, A. G., Strolger, L.-G., Tonry, J., et al. 2004, *ApJ*, 607, 665
 Rigault, M., Aldering, G., Kowalski, M., et al. 2015, *ApJ*, 802, 20
 Rigault, M., Copin, Y., Aldering, G., et al. 2013, *A&A*, 560, A66
 Roman, M., Hardin, D., Betoule, M., et al. 2017, arXiv:1706.07697
 Ross, A. J., Samushia, L., Howlett, C., et al. 2015, *MNRAS*, 449, 835
 Rubin, D., Aldering, G., Barbary, K., et al. 2015, *ApJ*, 813, 137
 Saha, A., Wang, Z., Matheson, T., et al. 2016, *Proc. SPIE*, 9910, 99100F
 Sako, M., Bassett, B., Becker, A. C., et al. 2014, arXiv:1401.3317
 Sako, M., Bassett, B., Connolly, B., et al. 2011, *ApJ*, 738, 162
 Schlafly, E. F., & Finkbeiner, D. P. 2011, *ApJ*, 737, 103
 Schlafly, E. F., Finkbeiner, D. P., Jurić, M., et al. 2012, *ApJ*, 756, 158
 Schlegel, D. J., Finkbeiner, D. P., & Davis, M. 1998, *ApJ*, 500, 525
 Scodreggio, M., Guzzo, L., Garilli, B., et al. 2018, *A&A*, 609, 84

- Scolnic, D., Casertano, S., Riess, A., et al. 2015, *ApJ*, 815, 117
- Scolnic, D., & Kessler, R. 2016, *ApJL*, 822, 35
- Scolnic, D., Rest, A., Riess, A., et al. 2014, *ApJ*, 795, 45
- Scolnic, D. M., Jones, D. O., Rest, A., et al. 2017, arXiv:1710.00845
- Skrutskie, M. F., Cutri, R. M., Stiening, R., et al. 2006, *AJ*, 131, 1163
- Smee, S. A., Gunn, J. E., Uomoto, A., et al. 2013, *AJ*, 146, 32
- Stritzinger, M. D., Phillips, M. M., Boldt, L. N., et al. 2011, *AJ*, 142, 156
- Sullivan, M., Conley, A., Howell, D. A., et al. 2010, *MNRAS*, 406, 782
- Sullivan, M., Guy, J., Conley, A., et al. 2011, *ApJ*, 737, 102
- Sullivan, M., Le Borgne, D., Pritchet, C. J., et al. 2006, *ApJ*, 648, 868
- Suzuki, N., Rubin, D., Lidman, C., et al. 2012, *ApJ*, 746, 85
- Tonry, J., & Davis, M. 1979, *AJ*, 84, 1511
- Tripp, R. 1998, *A&A*, 331, 815
- Uddin, S. A., Mould, J., Lidman, C., Ruhlmann-Kleider, V., & Zhang, B. R. 2017, *ApJ*, 848, 56
- Weinberg, D. H., Mortonson, M. J., Eisenstein, D. J., et al. 2013, *PhR*, 530, 87
- Wolf, R. C., D'Andrea, C. B., Gupta, R. R., et al. 2016, *ApJ*, 821, 115
- Zhang, B. R., Childress, M. J., Davis, T. M., et al. 2017, *MNRAS*, 471, 2254